Engineered Science
DOI: https://dx.doi.org/10.30919/es1050

Enhancing Vibration Problem of Temperature-Dependent Functionally Graded Cylindrical Microshells Using Magneto-Electro-Elastic Micropatches

Peyman Roodgar Saffari,[1,*] Jintara Lawongkerd,[1,*] Thira Jearsiripongkul,[2] Chanachai Thongchom,[3] Pouyan Roodgar Saffari[3] and Suraparb Keawsawasvong[4]

Abstract

This research offers a thorough theoretical investigation of the vibration behavior of functionally graded (FG) cylindrical microshells augmented with magneto-electro-elastic (MEE) micro patches, considering temperature-dependent material properties. The structure is further surrounded by a Pasternak elastic medium. Accurate modeling of structural behavior is achieved by employing the first-order shear deformation theory (FSDT). To account for the size effect, the modified strain gradient theory (MSGT) is employed. The analysis focuses on the temperature dispersion over the thickness of the micro-shell, examining three distinct profiles: uniform, harmonic non-uniform, and nonlinear. The FG core's material characteristics are temperature-dependent and distributed according to a power law. The associated equations of motion are generated by the application of Hamilton's principle and subsequently solved with the Galerkin technique to determine the natural frequencies. The impact of various parameters, including gradient index, length scale parameters, temperature variation, MEE patch characteristics, magnetic potential, Pasternak medium's parameters, and electric voltage on the free vibration behavior is thoroughly investigated. The findings of this study contribute to understanding the potential of MEE patches in enhancing the dynamic response of temperature-dependent FG cylindrical microshells, offering valuable insights for practical applications in micro-electro-mechanical systems (MEMS) and smart structures.

Keywords: Magneto-electro-elastic Patches; Temperature-dependency; Size Effect; Functionally Graded Microshells; Modified Strain Gradient Theory.
Received: 21 October 2023; Revised: 06 December 2023; Accepted: 08 December 2023.
Article type: Research article.

1. Introduction

The adaptability and strength of cylindrical shells make them a fundamental component in a myriad of industrial sectors, contributing to advancements in technology, infrastructure, and innovation across the globe. As engineering practices continue to evolve, cylindrical shells will undoubtedly play an essential role in addressing new challenges and driving progress in diverse applications.[1] Furthermore, the cylindrical shell is an efficient structural shape to carry internal pressure and external loads and resist buckling, which makes it ideal for many storage, transportation, infrastructure, and defense applications.[2] There are specific uses for micro and nano cylinders at the micro and nano sizes due to their high surface area-to-volume ratios. Small cylindrical shells made from biodegradable polymers can be loaded with pharmaceuticals and injected for sustained and targeted drug release in the body. Microactuators, which are typically cylindrical microshells, are used in microsystems and MEMS for accurate mechanical manipulation.[3]

For several decades, the comprehension and prediction of the mechanical properties of macroscopic systems have been predominantly based on classic concepts in continuum

[1] *Department of Civil Engineering, Thammasat School of Engineering, Faculty of Engineering, Thammasat University, Pathumthani, 12120, Thailand.*
[2] *Department of Mechanical Engineering, Thammasat School of Engineering, Faculty of Engineering, Thammasat University, Pathumthani, 12121, Thailand.*
[3] *Research Unit in Structural and Foundation Engineering, Department of Civil Engineering, Faculty of Engineering, Thammasat School of Engineering, Thammasat University, Pathumthani, 12120, Thailand.*

mechanics. For several decades, the comprehension and prediction of the mechanical properties of macroscopic systems have been predominantly based on classic concepts in continuum mechanics. To address these issues and provide more accurate predictions, researchers have turned to non-classical theories such as the nonlocal theory (NT) proposed by Eringen.[4,5] modified strain gradient theory (MSGT),[6] strain gradient theory (SGT),[7] modified couple stress theory (MCST),[8] and nonlocal strain gradient theory (NSGT).[9] Nonlocal interactions between material spots are considered by the NT, for instance, which allows for the consideration of long-range impacts and size-dependent dynamics.[10–15] The MSGT is characterized by three length-scale factors. The parameters utilized in the MSGT serve the purpose of incorporating size effects into the mechanical response of materials at small scales, namely in micro- and nanoscale constructions.[16] The MCST incorporates a single length-scale parameter. The utilization of this parameter is employed to consider the microstructural characteristics and coupled stresses that impact the mechanical response of materials at smaller scales.[17] The notion of NSGT is an amalgamation of NT and SGT, which serves to elucidate the influence of both nonlocality and strain gradients on the mechanical response of materials.[18–20] However, the utilization of molecular dynamics (MD) is a well-recognized computational methodology for the examination of the characteristics of micro- and nanostructures. Although MD simulations offer valuable insights into nanoscale processes, their computational requirements are substantial. This makes MD simulations impractical for studying large-scale systems with billions or trillions of atoms.[21] to address this difficulty, non-classical computational techniques have emerged as a viable and computationally efficient option for investigating nanoscale structures.[22]

Functionally graded materials (FGMs) are an innovative subset of engineered materials that have received a lot of interest in materials science and engineering. The volume of these materials varies continuously in composition, microstructure, and characteristics, allowing for the seamless integration of many functions.[23–32] The introduction of FGMs was initially proposed as a means to overcome the drawbacks associated with conventional materials, which typically exhibit stress concentration and diminished structural performance due to abrupt property transitions. As a result of their superior performance and durability in extreme conditions, FGMs have found widespread use in the aerospace industry, where they are included in a variety of aircraft components, turbine blades, and thermal protection systems. Heydari *et al*.[33] modeled the wave propagation in double-walled, air-filled, functionally graded cylindrical microshells under linear and nonlinear thermal loadings using a MSGT and a FSDT. Le *et al*.[34] developed an isogeometric analysis (IGA) technique to estimate the natural frequencies of the FG microshells based on the MSGT. Lyu *et al*.[35] conducted a study on the vibrational and buckling characteristics of a piezoelectric, porous cylindrical microshell made of FGMs. Zhao *et al*.[36] examined the natural frequency and elastic instability of a FG piezoelectric porous cylindrical microshell. Taghizadeh *et al*.[37] carried out the elastic instability of bi-directional FG conical micro-shells under axial loading employing MCST and FSDT. Mudhaffar *et al*.[38] investigated the effect of thermal loading on the bending behavior of a FG plate resting on a viscoelastic foundation. Furthermore, scholars have also conducted investigations on several thermal models in order to examine the static and dynamic characteristics of structures constructed from FGMs.[39–48]

Piezoelectric materials are widely recognized as a prominent category of smart materials due to their ability to produce electric charges in response to mechanical stress and, conversely, to generate mechanical strain when subjected to electric fields.[49] This unique property enables them to function as dual-purpose components, serving as both sensors and actuators. In contrast, magnetostrictive materials exhibit deformation in response to a magnetic field, rendering them well-suited for applications such as sensors, actuators, and vibration control systems.[50] Similarly to piezoelectric materials, electrostrictive materials may alter form in response to an applied electric field. This property has found application in precise positioning systems and micromanipulation.[51] Magneto-electro-elastic (MEE) materials have an interesting mix of magnetostrictive and piezoelectric characteristics. These materials are useful for sensors, transducers, and actuators because of their strain and electric polarization reactions to magnetic and electric fields.[52–56] Through a process of magneto-electric energy conversion, MEE materials can mitigate mechanical vibrations. Because of this, vibrations may be effectively muffled and dampened. Gui and Wu[57] conducted a study on the buckling characteristics of thermo-MEE cylindrical microshells that are incorporated into an elastic medium combining the Kirchhoff-Love theory with

[4] *Research Unit in* Sciences *and Innovative Technologies for Civil Engineering Infrastructures, Department of Civil Engineering, Faculty of Engineering, Thammasat School of Engineering, Thammasat University, Pathumthani, 12120, Thailand.*

**Email:* peyman.saffari1364@gmail.com, rpeyman@engr.tu.ac.th (P. R. Saffari), ljintara@engr.tu.ac.th (J. Lawongkerd)

the NSGT. Sirimontree *et al*..[58] employed the NT to investigate the vibroacoustic behavior of the MEE FG sandwich cylindrical nanoshell.

While previous studies have provided valuable insights into the dynamic performance of cylindrical micro- and nano shells made of FG and MEE smart materials, there remain deficiencies and shortcomings. Specifically, the free vibrations of a cylindrical sandwich microshell with an FG core and MEE patches have yet to be thoroughly analyzed using advanced theories like FSDT and MSGT. This represents a critical gap in current knowledge. Therefore, the present study aims to address this gap by investigating, for the first time, the free vibrations of such a cylindrical sandwich microshell system using FSDT and MSGT. The novel approach introduced here provides new perspectives and a deeper understanding of the vibration characteristics of these advanced cylindrical microshells. By providing new perspectives on the vibration characteristics of FG-MEE microshells, this work significantly advances current knowledge in this emerging research area. The structure is further surrounded by a Pasternak elastic medium. The novel contribution is the analysis of this specific shell configuration and material composition to further the fundamental understanding of vibrations in multifunctional microscale structures. The findings may have ramifications for the development and use of next-generation microscale devices that make use of superior grades and smart materials. There are three profiles taken into account for the temperature distribution over the microshell thickness: uniform, harmonic non-uniform, and nonlinear. The FG core's material characteristics are temperature-dependent and distributed according to a power law. In addition to filling a gap in the literature, the novel approach and findings of this study have important practical implications. Specifically, the vibrational analysis of cylindrical sandwich microshells presented here provides critical insights for the design and application of advanced microsystems and nanodevices. Cylindrical microshells with FG-MEE layers have promising applications in areas such as biomedical implants, drug delivery systems, micro actuators, and microsensors. By elucidating the vibration characteristics and dynamic stability of these structures, this work enables the more effective and optimized design of cylindrical microshell components for these technologies. The new knowledge contributed ~~in~~ to this study also aids in predicting and controlling the vibration response of FG-MEE cylindrical microshells when utilized in dynamic microsystems and nanostructures. Investigating the underlying linear dynamics through an analytical framework provides critical insights before examining nonlinear phenomena like large amplitude vibrations and geometric nonlinearities. Analysis of nonlinear dynamics and stability is outside the scope of the current study but represents an important and challenging area for future work.

2. Mathematical formulation

The geometry being examined, as seen in Fig. 1, is a circular cylindrical sandwich microshell with an FG core, having thickness denoted as h, radius R, and length L. As seen in the figure, the microshell is embedded within a Pasternak foundation characterized by shear stiffness denoted as K_{G} and Winkler stiffness represented by K_{W}. The core has a continuous variation in material composition described by a power-law volume fraction profile through the thickness. The core is integrated with Q periodically surface-bonded smart MEE patches made of $BaTiO_3$ and $CoFe_2O_4$ with thickness h_m and curvature angle ζ. Notably, the circumferential angle between two adjacent patches is $\beta = \frac{2\pi}{N} - \zeta$.

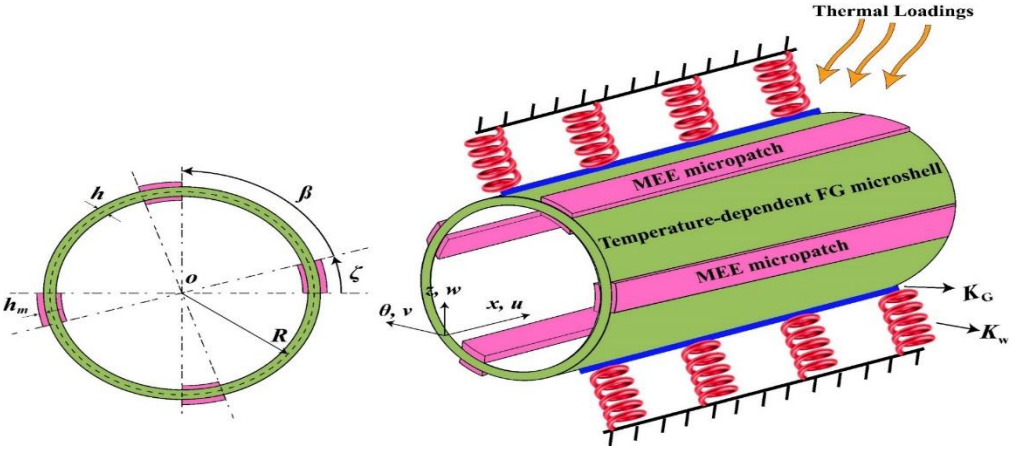

Fig. 1 Illustration of a circular cylindrical sandwich FG microshell integrated with periodically surface-bonded MEE micropatches under temperature environment.

2.1 Material characteristics of temperature-dependent FG core layer

The distinctive properties of FG microshells are evaluated by the changing volume fractions of metal and ceramic phases. These volume fractions vary progressively throughout the core layer's thickness according to a straightforward power-law model. In the FG core layer, the effectiveness of the local material characteristics, represented by the symbol 'G,' is highly dependent on the precise location. This material efficiency 'G' at any given location is determined by analyzing the volume fraction distribution of metal and ceramic phases, as well as their related properties. Gradual changes in material composition allow for the development of specialized features with the potential to improve structural performance and open up new avenues of application in engineering and technology.[59]

$$G(z,T) = G_{\mathrm{c}}(T)\chi_{\mathrm{c}}(z) + G_{\mathrm{m}}(T)\chi_{\mathrm{m}}(z), \tag{1}$$

This study examines the composition of the FG core layer, which consists of two materials: m, representing the metal component (specifically, SUS304 is selected for examination), and c, representing the ceramic component (Si3N4 is assumed for this inquiry). The characterization of the distribution of these two components, indicated as χ_{c} and χ_{m}, over the thickness of the core layer is based on their respective volume fractions. There is a one-to-one relationship between the percentages of each material (represented by G_{c} and G_{m}) and the volume fractions (χ_{c} and χ_{m}). The formula for this connection is as follows.[60]

$$\chi_{\mathrm{c}}(z) = \left(\frac{z}{h} + \frac{1}{2}\right)^{N}, \quad \chi_{\mathrm{c}}(z) + \chi_{\mathrm{m}}(x,y,z) = 1, \tag{2}$$

The equation takes into account the power law component, represented by the symbol N, which measures the extent of material change throughout the thickness of the core layer. In addition, the study incorporates the thermo-elastic properties of the material, considering the impact of temperature (T). The subsequent equation denotes the combined impact of the power law coefficient and temperature on the material behavior of the FG core layer.[59]

$$G(T) = G_0(G_{-1}T^{-1} + 1 + G_1T + G_2T^2 + G_3T^3), \tag{3}$$

The coefficients G_{-1}, G_0, G_1, G_2, and G_3 are influenced by the temperature T (in Kelvin) and represent various material properties such as mass density (ρ), thermal expansion coefficient (α), thermal conductivity (k), Young's modulus (E), and Poisson's ratio (ϑ). The coefficients display behavior contingent on temperature, and their quantities undergo variation with changes in temperature, as presented in Table 1. However, the practical material characteristics can be determined by employing equations (1) and (2) as:[61]

$$\begin{aligned}
E(z,T) &= [E_{\mathrm{c}}(T) - E_{\mathrm{m}}(T)]\left(\frac{z}{h} + \frac{1}{2}\right)^{N} + E_{\mathrm{m}}(T),\\
\rho(z,T) &= [\rho_{\mathrm{c}}(T) - \rho_{\mathrm{m}}(T)]\left(\frac{z}{h} + \frac{1}{2}\right)^{N} + \rho_{\mathrm{m}}(T),\\
\vartheta(z,T) &= [\vartheta_{\mathrm{c}}(T) - \vartheta_{\mathrm{m}}(T)]\left(\frac{z}{h} + \frac{1}{2}\right)^{N} + \vartheta_{\mathrm{m}}(T),\\
\alpha(z,T) &= [\alpha_{\mathrm{c}}(T) - \alpha_{\mathrm{m}}(T)]\left(\frac{z}{h} + \frac{1}{2}\right)^{N} + \alpha_{\mathrm{m}}(T),\\
k(z,T) &= [k_{\mathrm{c}}(T) - k_{\mathrm{m}}(T)]\left(\frac{z}{h} + \frac{1}{2}\right)^{N} + k_{\mathrm{m}}(T),
\end{aligned} \tag{4}$$

2.2 Temperature variation

Uniform distribution of temperature (UDT): The sandwich microshell is assumed to have a uniform distribution of temperature, indicating that it has achieved thermal equilibrium over time when subjected to a constant ambient temperature. This allows the temperature field to be modeled as spatially invariant along the thickness direction, despite its graded material composition.[62]

$$T(z) = T_0 + \Delta T, \quad \Delta T = T_{\mathrm{c}} - T_{\mathrm{m}}. \tag{5}$$

In the current investigation, the structure is assumed to be initially stress-free, corresponding to the ambient temperature T_0.

Harmonic temperature rise (HTR): In the second case, the variation of thickness with temperature is prescribed to follow a sinusoidal pattern, which can be expressed mathematically as:[63]

$$T(z) = (T_{\mathrm{c}} - T_{\mathrm{m}})\left(1 - \cos\left[\frac{\pi}{2}\left(\left(\frac{z}{h} + \frac{1}{2}\right)\right)\right]\right) + T_{\mathrm{m}}. \tag{6}$$

Nonlinear temperature distribution (NTD): The utilization of the steady-state Fourier heat conduction technique enables the computation of the nonlinear temperature distribution in a sandwich microshell. Due to its thermal characteristics and material gradient, the FG core layer may be evaluated with excellent accuracy utilizing heat conduction principles.[64]

$$-\frac{\partial}{\partial z}\left(k(z,T)\frac{\partial T}{\partial z}\right) = 0, \quad T\left(\frac{h}{2}\right) = T_{\mathrm{c}}, \quad T\left(-\frac{h}{2}\right) = T_{\mathrm{m}}. \tag{7}$$

The solution to equation (7) may be derived by solving the polynomial series while considering the provided boundary conditions in the following manner.[65]

$$T(z) = T_{\mathrm{m}} + (T_{\mathrm{c}} - T_{\mathrm{m}})\Gamma(z),$$

$$\Gamma(z) = \frac{1}{\Psi}\left[\left(\frac{z}{h} + \frac{1}{2}\right) - \frac{\kappa_{cm}}{(N+1)k_{\mathrm{m}}}\left(\frac{z}{h} + \frac{1}{2}\right)^{N+1} + \frac{{\kappa_{cm}}^2}{(N+1){k_m}^2}\left(\frac{z}{h} + \frac{1}{2}\right)^{2N+1} - \frac{{\kappa_{cm}}^3}{(N+1){k_m}^3}\left(\frac{z}{h} + \frac{1}{2}\right)^{3N+1} + \frac{{\kappa_{cm}}^4}{(N+1){k_m}^4}\left(\frac{z}{h} + \frac{1}{2}\right)^{4N+1} - \frac{{\kappa_{cm}}^5}{(N+1){k_m}^5}\left(\frac{z}{h} + \frac{1}{2}\right)^{5N+1}\right],$$

$$\Psi = 1 - \frac{\kappa_{cm}}{(N+1)k_m} + \frac{{\kappa_{cm}}^2}{(2N+1){k_m}^2} - \frac{{\kappa_{cm}}^3}{(3N+1){k_m}^3} + \frac{{\kappa_{cm}}^4}{(4N+1){k_m}^4} -$$

$$\frac{{\kappa_{cm}}^5}{(5N+1){k_m}^5}, \kappa_{cm} = k_c - k_m. \quad (8)$$

2.3 MEE patch fundamental relations

The construction of all MEE patches involves the utilization of CoFe2O4 and BaTiO3 materials. Subsequently, a comprehensive description is provided for each MEE layer, including the electric displacement D, magnetic induction B, and stress tensor σ, while taking into account the temperature environment.[66]

$$\begin{bmatrix}\sigma_{xxi}\\ \sigma_{\theta\theta i}\\ \tau_{x\theta i}\\ \tau_{\theta zi}\\ \tau_{xzi}\end{bmatrix}_{\text{MEE}} = \begin{Bmatrix}c_{11} & c_{12} & 0 & 0 & 0\\ c_{12} & c_{22} & 0 & 0 & 0\\ 0 & 0 & c_{44} & 0 & 0\\ 0 & 0 & 0 & c_{55} & 0\\ 0 & 0 & 0 & 0 & c_{66}\end{Bmatrix}\begin{bmatrix}\varepsilon_{xx}\\ \varepsilon_{\theta\theta}\\ \gamma_{x\theta}\\ \gamma_{\theta z}\\ \gamma_{xz}\end{bmatrix} - \begin{Bmatrix}0 & 0 & e_{31}\\ 0 & 0 & e_{32}\\ 0 & e_{24} & 0\\ e_{15} & 0 & 0\\ 0 & 0 & 0\end{Bmatrix}\begin{bmatrix}\mathrm{E}_{xi}\\ \mathrm{E}_{\theta i}\\ \mathrm{E}_{zi}\end{bmatrix} - \begin{Bmatrix}0 & 0 & q_{31}\\ 0 & 0 & q_{32}\\ 0 & q_{24} & 0\\ q_{15} & 0 & 0\\ 0 & 0 & 0\end{Bmatrix}\begin{bmatrix}\mathcal{H}_{xi}\\ \mathcal{H}_{\theta i}\\ \mathcal{H}_{zi}\end{bmatrix} - \begin{bmatrix}\lambda_1\\ \lambda_2\\ 0\\ 0\\ 0\end{bmatrix}\Delta T,$$

$$\begin{bmatrix}D_{xi}\\ D_{\theta i}\\ D_{zi}\end{bmatrix} = \begin{Bmatrix}0 & 0 & e_{31}\\ 0 & 0 & e_{32}\\ 0 & e_{24} & 0\\ e_{15} & 0 & 0\\ 0 & 0 & 0\end{Bmatrix}^T\begin{bmatrix}\varepsilon_{xx}\\ \varepsilon_{\theta\theta}\\ \gamma_{x\theta}\\ \gamma_{\theta z}\\ \gamma_{xz}\end{bmatrix} + \begin{Bmatrix}\kappa_{11} & 0 & 0\\ 0 & \kappa_{22} & 0\\ 0 & 0 & \kappa_{33}\end{Bmatrix}\begin{bmatrix}\mathrm{E}_{xi}\\ \mathrm{E}_{\theta i}\\ \mathrm{E}_{zi}\end{bmatrix} + \begin{Bmatrix}a_{11} & 0 & 0\\ 0 & a_{22} & 0\\ 0 & 0 & a_{33}\end{Bmatrix}\begin{bmatrix}\mathcal{H}_{xi}\\ \mathcal{H}_{\theta i}\\ \mathcal{H}_{zi}\end{bmatrix} + \begin{bmatrix}p_1\\ p_2\\ p_3\end{bmatrix}\Delta T, \quad (9)$$

$$\begin{bmatrix}B_{xi}\\ B_{\theta i}\\ B_{zi}\end{bmatrix} = \begin{Bmatrix}0 & 0 & q_{31}\\ 0 & 0 & q_{32}\\ 0 & q_{24} & 0\\ q_{15} & 0 & 0\\ 0 & 0 & 0\end{Bmatrix}^T\begin{bmatrix}\varepsilon_{xx}\\ \varepsilon_{\theta\theta}\\ \gamma_{x\theta}\\ \gamma_{\theta z}\\ \gamma_{xz}\end{bmatrix} + \begin{Bmatrix}a_{11} & 0 & 0\\ 0 & a_{22} & 0\\ 0 & 0 & a_{33}\end{Bmatrix}\begin{bmatrix}\mathrm{E}_{xi}\\ \mathrm{E}_{\theta i}\\ \mathrm{E}_{zi}\end{bmatrix} + \begin{Bmatrix}\mu_{11} & 0 & 0\\ 0 & \mu_{22} & 0\\ 0 & 0 & \mu_{33}\end{Bmatrix}\begin{bmatrix}\mathcal{H}_{xi}\\ \mathcal{H}_{\theta i}\\ \mathcal{H}_{zi}\end{bmatrix} + \begin{bmatrix}q_1\\ q_2\\ q_3\end{bmatrix}\Delta T, \quad i = \text{in, ex.}$$

where in and ex represent the MEE patches on the inside and outside, respectively. The normal strain components are denoted as ε_{xx} and $\varepsilon_{\theta\theta}$, whereas the shear strain components are represented by $\gamma_{x\theta}$, γ_{xz}, and $\gamma_{\theta z}$. The elasticity tensor, magnetic constants, dielectric, magnetoelectric, piezomagnetic, and piezoelectric components are also denoted by the symbols $[c], [\mu], [a], [\kappa], [q], [e]$, and $[e]$ respectively, which can be presented as:[66]

$$c_{11} = \bar{c}_{11} - \frac{{\bar{c}_{13}}^2}{\bar{c}_{33}}, \quad c_{12} = \bar{c}_{12} - \frac{\bar{c}_{13}\bar{c}_{23}}{\bar{c}_{33}}, \quad c_{22} = \bar{c}_{22} - \frac{{\bar{c}_{23}}^2}{\bar{c}_{33}}, \quad c_{44} = \bar{c}_{44}, \quad c_{55} = \bar{c}_{55},$$

$$c_{66} = \bar{c}_{66}, \ e_{31} = \bar{e}_{31} - \frac{\bar{c}_{13}\bar{e}_{33}}{\bar{c}_{33}}, \ e_{32} = \bar{e}_{32} - \frac{\bar{c}_{23}\bar{e}_{33}}{\bar{c}_{33}}, \quad (10)$$

$$e_{24} = \bar{e}_{24}, \ e_{15} = \bar{e}_{15}, \ q_{31} = \bar{q}_{31} - \frac{\bar{c}_{13}\bar{q}_{33}}{\bar{c}_{33}},$$

$$q_{32} = \bar{q}_{32} - \frac{\bar{c}_{23}\bar{q}_{33}}{\bar{c}_{33}}, \ q_{24} = \bar{q}_{24}, \ q_{15} = \bar{q}_{15},$$

$$k_{11} = \bar{k}_{11}, \ k_{22} = \bar{k}_{11}, \ k_{33} = \bar{k}_{33} + \frac{{\bar{e}_{33}}^2}{\bar{c}_{33}}, \ a_{11} = \bar{a}_{11},$$

$$a_{22} = \bar{a}_{22}, \ a_{33} = \bar{a}_{33} + \frac{\bar{q}_{33}\bar{e}_{33}}{\bar{c}_{33}}, \ \mu_{11} = \bar{\mu}_{11},$$

$$\mu_{22} = \bar{\mu}_{22},$$

$$\mu_{33} = \bar{\mu}_{33} + \frac{{q_{33}}^2}{C_{33}}, \lambda_1 = \bar{\lambda}_1 - \frac{\bar{c}_{13}\lambda_3}{\bar{c}_{33}}, \ \lambda_2 = \bar{\lambda}_1 - \frac{\bar{c}_{23}\lambda_3}{\bar{c}_{33}},$$

However, in equation (9), $[\mathcal{H}]$ and [E] represent the magnetic and electric fields that are generated by magnetic and electric potentials, respectively. The magnetic field vector may be determined by evaluating the negative gradient of the magnetic potential function (Ψ). In a similar vein, the electric field vector may be obtained by differentiating the electric potential function (Φ).[67]

$$(E_x, \mathcal{H}_x) = -\frac{\partial}{\partial x}(\Phi, \Psi),$$

$$(E_\theta, \mathcal{H}_\theta) = -\frac{1}{R+z}\frac{\partial}{\partial \theta}(\Phi, \Psi),$$

$$(E_z, \mathcal{H}_z) = -\frac{\partial}{\partial z}(\Phi, \Psi) \quad (11)$$

The present study presents a commonly employed approach for characterizing the variations in electric and magnetic potentials along the thickness direction of internal and exterior MEE patches as:[67,68]

$$\Phi_{\text{ex}}(x,\theta,z,t) = \left[\left(z - \frac{h+h_m}{2}\right)^2 - \left(\frac{h_m}{2}\right)^2\right]\bar{\Phi}_{\text{ex}}(x,\theta,t) + 2\left(z - \frac{h+h_m}{2}\right)V_0,$$

$$\Phi_{\text{in}}(x,\theta,z,t) = \left[\left(z + \frac{h+h_m}{2}\right)^2 - \left(\frac{h_m}{2}\right)^2\right]\bar{\Phi}_{\text{in}}(x,\theta,t) + 2\left(z + \frac{h+h_m}{2}\right)V_0, \quad (12)$$

$$\Psi_{\text{ex}}(x,\theta,z,t) = \left[\left(z - \frac{h+h_m}{2}\right)^2 - \left(\frac{h_m}{2}\right)^2\right]\bar{\Psi}_{\text{ex}}(x,\theta,t) + 2\left(z - \frac{h+h_m}{2}\right)\Gamma_0,$$

$$\Psi_{\text{in}}(x,\theta,z,t) = \left[\left(z+\frac{h+h_m}{2}\right)^2 - \left(\frac{h_m}{2}\right)^2\right]\bar{\Psi}_{\text{in}}(x,\theta,t) + 2\left(z+\frac{h+h_m}{2}\right)\Gamma_0,$$

It is assumed that each internal and external smart patch has the same electric voltage (V_0) and initial magnetic potential (Γ_0). Furthermore, $\bar{\Phi}$ and $\bar{\Psi}$ refer to the two-dimensional electric and magnetic potentials.

2.4 MSGT

MSGT is a sophisticated mathematical framework that goes beyond traditional strain gradient theory to give a more in-depth understanding of material behavior at small scales. The utilization of gradient tensors in the context of MSGT is of utmost importance as it enables a precise depiction of the deformation and strain properties of materials, especially within micro- and nanostructural domains.[6] The strain energy ($\Xi_{\mathcal{V}}$) for a linear elastic continuum experiencing tiny deformations can be expressed as shown in Ref. [6]

$$\Xi_{\mathcal{V}} = 1/2\int_{\Omega}\left(\sigma_{ij}\varepsilon_{ij} + p_i\gamma_i + \tau^{(1)}_{ijk}\eta^{(1)}_{ijk} + m^s_{ij}\mathrm{X}^s_{ij}\right)dv \quad (13)$$

where the dilatation gradient, deviatoric stretch gradient, strain, and symmetric rotation gradient tensors are represented by the variables γ_i, $\eta^{(1)}_{ijk}$, X^s_{ij}, and ε_{ij}, respectively. Furthermore, the classical stress tensor is denoted by σ, while the higher-order stresses are represented by p_i, $\tau^{(1)}_{ijk}$, and m^s_{ij} as:[6]

$$\sigma_{ij} = \lambda\varepsilon_{kk}\delta_{ij} + 2\mu\varepsilon_{ij} - \alpha(z,T)\Delta T,$$
$$p_i = 2\mu {l_0}^2\gamma_i,$$
$$\tau^{(1)}_{ijk} = 2\mu {l_1}^2\mu\eta^{(1)}_{ijk}, \quad (14)$$

$m^s_{ij} = 2\mu {l_2}^2\mathrm{X}^s_{ij}$where μ and λ denote shear and bulk modules, respectively. Independent material length scale parameters for symmetric rotation, deviatoric stretch, and dilatation are also indicated by the parameters l_2, l_1, and l_0. The aforementioned length-scale factors play a pivotal role in the characterization of material behavior and the inclusion of size-dependent effects within the examined continuum.

$$\varepsilon_{ij} = \frac{1}{2}\left(u_{i,j} + u_{j,i}\right),$$
$$\gamma_i = \varepsilon_{mm,i},$$
$$\eta^{(1)}_{ijk} = \eta^{(1)}_{ijk} = \eta^s_{ijk} - \frac{1}{5}\left(\delta_{ij}\eta^s_{mmk} + \delta_{jk}\eta^s_{mmi} + \delta_{ki}\eta^s_{mmj}\right); \eta^s_{ijk} = \frac{1}{3}\left(\varepsilon_{jk,i} + \varepsilon_{ki,j} + \varepsilon_{ij,k}\right), \quad (15)$$
$$\mathrm{X}^s_{ij} = \frac{1}{2}\left(\varrho_{i,j} + \varrho_{j,i}\right); \varrho_i = \frac{1}{2}(\mathrm{curl}(\boldsymbol{u}))_i$$

The variable u represents the constituent parts of the displacement vector. In the context being discussed, the symbol ϱ is applied to symbolize the infinitesimal rotation vector, whereas the symbol δ is utilized to indicate the Kronecker delta.

2.5 Constitutive relations

The FSDT takes into account the presence of a continuous transverse shear deformation, which is in contrast to the stress-free state experienced by the top and lower surfaces of the microshell. The incorporation of a shear correction factor is imperative in the framework of the FSDT in order to accommodate the adjustment of transverse shear forces. Within the theoretical framework of this study, the displacement field for the sandwich microshell is conceptualized and modeled as:[69]

$$u_x(x,\theta,z,t) = u(x,\theta,t) + z\psi_x(x,\theta,t),$$
$$u_\theta(x,\theta,z,t) = v(x,\theta,t) + z\psi_\theta(x,\theta,t), \quad (16)$$
$$u_z(x,\theta,z,t) = w(x,\theta,t),$$

in which the microshell's normals, ψ_θ and ψ_x, display transverse rotations about the θ and x axes. Furthermore, w, v, and u indicate the displacements in the z, θ, and x directions of a point located in the center of the plane of microshell. The determination of strains within the microshell structure may be obtained by applying the fundamental principles of linear elasticity theory. This technique is predicated on a series of underlying assumptions, which can be outlined as follows:[69]

$$\varepsilon_{xx} = \frac{\partial u}{\partial x} + z\frac{\partial\psi_x}{\partial x},$$
$$\varepsilon_{\theta\theta} = \frac{1}{R}\frac{\partial v}{\partial\theta} + \frac{z}{R}\frac{\partial\psi_\theta}{\partial\theta} + \frac{w}{R},$$
$$\gamma_{x\theta} = \frac{\partial v}{\partial x} + \frac{1}{R}\frac{\partial u}{\partial\theta} + z\left(\frac{1}{R}\frac{\partial\psi_x}{\partial\theta} + \frac{\partial\psi_\theta}{\partial x}\right), \quad (17)$$
$$\gamma_{\theta z} = \psi_\theta + \frac{1}{R}\frac{\partial w}{\partial\theta} - \frac{v}{R},$$
$$\gamma_{xz} = \frac{\partial w}{\partial x} + \psi_x.$$

The values of the non-zero components X^s_{ij}, γ_i, and $\eta^{(1)}_{ijk}$ (where $i,j,k = x,\theta,z$) for sandwich microshell may be derived by substituting equations (16) and (17) into equations (15), which can be presented in **Appendix A**. The governing equations that describe the vibration behavior of an FG MEE sandwich microshell as a function of temperature and size may

be derived using Hamilton's principle.[70,71]

$$\int_{t_0}^{t}(\delta\Xi_{\mathcal{T}}-\delta\Xi_{\mathcal{V}}+\delta\Xi_{\mathcal{W}})dt=0. \tag{18}$$

In the present framework, the variable $\Xi_{\mathcal{W}}$ represents the virtual work carried out by a temperature gradient, initial magnetic potential, and electric voltage. In the context being discussed, the variable $\Xi_{\mathcal{V}}$ represents the virtual strain energy, whereas $\Xi_{\mathcal{T}}$ is used to describe the virtual kinetic energy. The equation representing a variation in kinetic energy may be expressed in the following manner:

$$\delta\Xi_{\mathcal{T}}=\int_x\Big[I_0\Big(\frac{\partial u}{\partial t}\frac{\partial\delta u}{\partial t}+\frac{\partial v}{\partial t}\frac{\partial\delta v}{\partial t}+\frac{\partial w}{\partial t}\frac{\partial\delta w}{\partial t}\Big)+I_1\Big(\frac{\partial u}{\partial t}\frac{\partial\delta\psi_x}{\partial t}+\frac{\partial v}{\partial t}\frac{\partial\delta\psi_\theta}{\partial t}+\frac{\partial\psi_x}{\partial t}\frac{\partial\delta u}{\partial t}+\frac{\partial\psi_\theta}{\partial t}\frac{\partial\delta v}{\partial t}\Big)+I_2\Big(\frac{\partial\psi_x}{\partial t}\frac{\partial\delta\psi_x}{\partial t}+\frac{\partial\psi_\theta}{\partial t}\frac{\partial\delta\psi_\theta}{\partial t}\Big)\Big]\,\mathrm{d}x \tag{19}$$

where ρ_{MEE} denotes the mass density of MEE patch, and the mass inertias are provided in the following manner

$$[I_0,I_1,I_2]=\sum_{\gamma=1}^{Q}\int_{(\gamma-1)(\zeta+\beta)}^{\gamma\zeta+(\gamma-1)\beta}\int_{-\frac{h}{2}-h_m}^{-\frac{h}{2}}\rho_{\mathrm{MEE}}\,[1,z,z^2]dzd\theta+\int_0^{2\pi}\int_{-\frac{h}{2}}^{\frac{h}{2}}\rho(z,T)\,[1,z,z^2]dzd\theta+\sum_{\gamma=1}^{Q}\int_{(\gamma-1)(\zeta+\beta)}^{\gamma\zeta+(\gamma-1)\beta}\int_{\frac{h}{2}}^{\frac{h}{2}+h_m}\rho_{\mathrm{MEE}}[1,z,z^2]\,dzd\theta \tag{20}$$

Plugging in equations (14) and (17) into equation (13) results in the subsequent mathematical equation for the strain energy variation:

$$\begin{aligned}\delta\Xi_{\mathcal{V}}=\sum_{\gamma=1}^{Q}\int_x\int_{(\gamma-1)(\zeta+\beta)}^{\gamma\zeta+(\gamma-1)\beta}\int_{-\frac{h}{2}-h_m}^{-\frac{h}{2}}\Big(&\sigma_{xx\mathrm{in}}\delta\varepsilon_{xx}+\sigma_{\theta\theta\mathrm{in}}\delta\varepsilon_{\theta\theta}+\tau_{\theta z\mathrm{in}}\delta\gamma_{\vartheta z}+\tau_{xz\mathrm{in}}\delta\gamma_{xz}+\tau_{x\theta\mathrm{in}}\delta\gamma_{x\theta}+p_x\delta\gamma_x+\\&p_\theta\delta\gamma_\theta+p_z\delta\gamma_z+\tau_{xxx}^{(1)}\delta\eta_{xxxf}^{(1)}+\tau_{\theta\theta\theta}^{(1)}\delta\eta_{\theta\theta\theta}^{(1)}+\tau_{zzz}^{(1)}\delta\eta_{zzz}^{(1)}+\\&\tau_{xx\theta}^{(1)}\delta\eta_{xx\theta}^{(1)}+\tau_{x\theta x}^{(1)}\delta\eta_{x\theta x}^{(1)}+\tau_{\theta xx}^{(1)}\delta\eta_{\theta xx}^{(1)}+\tau_{xzz}^{(1)}\delta\eta_{xzz}^{(1)}+\\&\tau_{xzx}^{(1)}\delta\eta_{xzx}^{(1)}+\tau_{zxx}^{(1)}\delta\eta_{zxx}^{(1)}+\tau_{\theta\theta x}^{(1)}\delta\eta_{\theta\theta x}^{(1)}+\tau_{\theta x\theta}^{(1)}\delta\eta_{\theta x\theta}^{(1)}+\\&\tau_{x\theta\theta}^{(1)}\delta\eta_{x\theta\theta}^{(1)}+\tau_{\theta\theta z}^{(1)}\delta\eta_{\theta\theta z}^{(1)}+\tau_{\theta z\theta}^{(1)}\delta\eta_{\theta z\theta}^{(1)}+\tau_{z\theta\theta}^{(1)}\delta\eta_{z\theta\theta}^{(1)}+\\&\tau_{zzx}^{(1)}\delta\eta_{zzx}^{(1)}+\tau_{zxzf}^{(1)}\delta\eta_{zxzf}^{(1)}+\tau_{xzzf}^{(1)}\delta\eta_{xzzf}^{(1)}+\tau_{zz\theta}^{(1)}\delta\eta_{zz\theta}^{(1)}+\\&\tau_{z\theta z}^{(1)}\delta\eta_{z\theta z}^{(1)}+\tau_{\theta zz}^{(1)}\delta\eta_{\theta zz}^{(1)}+\tau_{x\theta z}^{(1)}\delta\eta_{x\theta z}^{(1)}+\tau_{\theta xz}^{(1)}\delta\eta_{\theta xz}^{(1)}+\\&\tau_{zx\theta}^{(1)}\delta\eta_{zx\theta}^{(1)}+\tau_{z\theta x}^{(1)}\delta\eta_{z\theta x}^{(1)}+m_{xx}^{s}\delta\mathrm{X}_{xx}^{s}+m_{\theta\theta}^{s}\delta\mathrm{X}_{\theta\theta}^{s}+\\&m_{zz}^{s}\delta\mathrm{X}_{zz}^{s}+m_{x\theta}^{s}\delta\mathrm{X}_{x\theta}^{s}+m_{xz}^{s}\delta\mathrm{X}_{xz}^{s}+m_{\theta z}^{s}\delta\mathrm{X}_{\theta z}^{s}-\\&D_{x\mathrm{in}}\delta\mathrm{E}_{x\mathrm{in}}-D_{\theta\mathrm{in}}\delta\mathrm{E}_{\theta\mathrm{in}}-D_{z\mathrm{in}}\delta\mathrm{E}_{z\mathrm{in}}-B_{x\mathrm{in}}\delta\mathcal{H}_{x\mathrm{in}}-\\&B_{\theta\mathrm{in}}\delta\mathcal{H}_{\theta\mathrm{in}}-B_{z\mathrm{in}}\delta\mathcal{H}_{z\mathrm{in}}\Big)_{\mathrm{MEE}}\,\mathrm{d}z\mathrm{d}\theta\mathrm{d}x+\\\int_x\int_0^{2\pi}\int_{-\frac{h}{2}}^{\frac{h}{2}}\Big(&\sigma_{xx}^{\mathrm{FGM}}\varepsilon_{xx}+\sigma_{\theta\theta}^{\mathrm{FGM}}\delta\varepsilon_{\theta\theta}+\tau_{x\theta}^{\mathrm{FGM}}\delta\gamma_{x\theta}+\tau_{xz}^{\mathrm{FGM}}\delta\gamma_{xz}+\tau_{\theta z}^{\mathrm{FGM}}\delta\gamma_{\theta z}+p_x\delta\gamma_x+p_\theta\delta\gamma_\theta+p_z\delta\gamma_z+\\&\tau_{xxx}^{(1)}\delta\eta_{xxxf}^{(1)}+\tau_{\theta\theta\theta}^{(1)}\delta\eta_{\theta\theta\theta}^{(1)}+\tau_{zzz}^{(1)}\delta\eta_{zzz}^{(1)}+\tau_{xx\theta}^{(1)}\delta\eta_{xx\theta}^{(1)}+\\&\tau_{x\theta x}^{(1)}\delta\eta_{x\theta x}^{(1)}+\tau_{\theta xx}^{(1)}\delta\eta_{\theta xx}^{(1)}+\tau_{xxz}^{(1)}\delta\eta_{xxz}^{(1)}+\tau_{xzx}^{(1)}\delta\eta_{xzx}^{(1)}+\\&\tau_{zxx}^{(1)}\delta\eta_{zxx}^{(1)}+\tau_{\theta\theta x}^{(1)}\delta\eta_{\theta\theta x}^{(1)}+\tau_{\theta x\theta}^{(1)}\delta\eta_{\theta x\theta}^{(1)}+\\&\tau_{x\theta\theta}^{(1)}\delta\eta_{x\theta\theta}^{(1)}+\tau_{\theta\theta z}^{(1)}\delta\eta_{\theta\theta z}^{(1)}+\tau_{\theta z\theta}^{(1)}\delta\eta_{\theta z\theta}^{(1)}+\tau_{z\theta\theta}^{(1)}\delta\eta_{z\theta\theta}^{(1)}+\\&\tau_{zzx}^{(1)}\delta\eta_{zzx}^{(1)}+\tau_{zxzf}^{(1)}\delta\eta_{zxzf}^{(1)}+\tau_{xzzf}^{(1)}\delta\eta_{xzzf}^{(1)}+\tau_{zz\theta}^{(1)}\delta\eta_{zz\theta}^{(1)}+\\&\tau_{z\theta z}^{(1)}\delta\eta_{z\theta z}^{(1)}+\tau_{\theta zz}^{(1)}\delta\eta_{\theta zz}^{(1)}+\tau_{x\theta z}^{(1)}\delta\eta_{x\theta z}^{(1)}+\tau_{\theta xz}^{(1)}\delta\eta_{\theta xz}^{(1)}+\\&\tau_{zx\theta}^{(1)}\delta\eta_{zx\theta}^{(1)}+\tau_{z\theta x}^{(1)}\delta\eta_{z\theta x}^{(1)}+m_{xx}^{s}\delta\mathrm{X}_{xx}^{s}+m_{\theta\theta}^{s}\delta\mathrm{X}_{\theta\theta}^{s}+\\&m_{zz}^{s}\delta\mathrm{X}_{zz}^{s}+m_{x\theta}^{s}\delta\mathrm{X}_{x\theta}^{s}+m_{xz}^{s}\delta\mathrm{X}_{xz}^{s}+m_{\theta z}^{s}\delta\mathrm{X}_{\theta z}^{s}-\\&D_{x\mathrm{ex}}\delta\mathrm{E}_{x\mathrm{ex}}-D_{\theta\mathrm{ex}}\delta\mathrm{E}_{\theta\mathrm{ex}}-D_{z\mathrm{ex}}\delta\mathrm{E}_{z\mathrm{ex}}-B_{x\mathrm{ex}}\delta\mathcal{H}_{x\mathrm{ex}}-\\&B_{\theta\mathrm{ex}}\delta\mathcal{H}_{\theta\mathrm{ex}}-B_{z\mathrm{ex}}\delta\mathcal{H}_{z\mathrm{ex}}\Big)_{\mathrm{MEE}}\,\mathrm{d}z\mathrm{d}\theta\mathrm{d}x\end{aligned} \tag{21}$$

Finally, the virtual work resulting from the temperature environment, Pasternak medium, as well as the initial electric and magnetic potentials, may be described in the following manner:

$$\delta\Xi_{\mathcal{W}}=\int_A\Big\{-K_{\mathrm{W}}w\delta w+(N_x^E+N_x^M+N_x^T+K_G)\frac{\partial w}{\partial x}\delta\frac{\partial w}{\partial x}+\frac{1}{R^2}\big(N_\theta^E+N_\theta^M+N_\theta^T+K_G\big)\frac{\partial w}{\partial\theta}\delta\frac{\partial w}{\partial\theta}\Big\}\mathrm{d}A,$$

$$N_x^T=\int_{-h_{\mathrm{m}}-h/2}^{-h/2}\lambda_1\Delta T dz+\int_{-\frac{h}{2}}^{\frac{h}{2}}\frac{E(z,T)}{1-\vartheta(z,T)}\alpha(z,T)\Delta T dz+$$

$$\int_{h/2}^{h/2+h_m} \lambda_1 \Delta T dz dz, \quad (22)$$

$$N_\theta^T = \int_{-h_m-h/2}^{-h/2} \lambda_2 \Delta T dz + \int_{-\frac{h}{2}}^{\frac{h}{2}} \frac{E(z,T)}{1-\vartheta(z,T)} \alpha(z,T) \Delta T dz + \int_{h/2}^{h/2+h_m} \lambda_2 \Delta T dz dz ,$$

$$N_{xx}^E = \int_{\frac{h}{2}}^{\frac{h}{2}+h_m} 2e_{31}V_0/h_m dz , \; N_{\theta\theta}^E = \int_{\frac{h}{2}}^{\frac{h}{2}+h_m} 2e_{32}V_0/h_m dz ,$$

$$N_{xx}^M = \int_{\frac{h}{2}}^{\frac{h}{2}+h_m} 2q_{31}\Gamma_0/h_m dz , \; N_{\theta\theta}^M = \int_{\frac{h}{2}}^{\frac{h}{2}+h_m} 2q_{32}\Gamma_0/h_m dz ,$$

The governing equations based on the FSDT are obtained by replacing equations (19), (21), and (22) into equation (18), doing some additional computations, and understanding that coefficients $\delta u, \delta v, \delta w, \delta\psi_x, \delta\psi_\theta, \delta\bar{\Phi}_{ex}, \delta\bar{\Phi}_{in}, \delta\bar{\Psi}_{ex}$, and $\delta\bar{\Psi}_{in}$ are all equal to zero, as presented in **Appendix B**.

3. The Galerkin technique

In this particular section, the utilization of the Galerkin technique results in analytical answers for the natural frequencies of the cylindrical sandwich FG microshell that has been improved using MEE patches. These solutions are applicable to a range of different boundary conditions. The below formulas may be employed to characterize the boundary conditions associated with clamped and simply supported edges:

Simply supported (S):

$$v = w = \theta_y = N_{xx} = M_{xx} = 0, \quad at\ x = 0, L. \quad (23)$$

Clamped (C):

$$u = v = w = \psi_x = \psi_\theta = 0, \quad at\ x = 0, L. \quad (24)$$

The subsequent displacement fields are employed to satisfy the corresponding boundary conditions.[72,73]

$$\langle u, \psi_x \rangle = \sum_m^\infty \sum_n^\infty \langle \bar{\bar{u}}, \bar{\bar{\psi}}_x \rangle \frac{\partial X_m(x)}{\partial x} \cos(n\theta) e^{i\omega t},$$

$$\langle v, \psi_\theta \rangle = \sum_m^\infty \sum_n^\infty \langle \bar{\bar{v}}, \bar{\bar{\psi}}_\theta \rangle X_m(x) \sin(n\theta) e^{i\omega t}, \quad (25)$$

$$\langle w, \bar{\Phi}_{in}, \bar{\Phi}_{ex}, \bar{\Psi}_{in}, \bar{\Psi}_{ex} \rangle = \sum_m^\infty \sum_n^\infty \langle \bar{\bar{w}}, \bar{\bar{\Phi}}_{in}, \bar{\bar{\Phi}}_{ex}, \bar{\bar{\Psi}}_{in}, \bar{\bar{\Psi}}_{ex} \rangle X_m(x) \cos(n\theta) e^{i\omega t},$$

where the values of m and n correspond to the half-wave numbers in the x and θ directions, and ω refers to the natural frequency of the structure. Furthermore, the variables $\bar{\bar{u}}, \bar{\bar{\psi}}_x, \bar{\bar{v}}, \bar{\bar{\psi}}_\theta, \bar{\bar{w}}, \bar{\bar{\Phi}}_{in}, \bar{\bar{\Phi}}_{ex}, \bar{\bar{\Psi}}_{in}, \bar{\bar{\Psi}}_{ex}$ represent the unknown modal coefficients. The axial modal function, denoted as $X_m(x)$, is chosen as a shell function that is expressed in the following manner:

$$X_m(x) = a_1 \cosh\left(\frac{\Xi_m x}{L}\right) + a_2 \cos\left(\frac{\Xi_m x}{L}\right) - \Omega_m \left[a_3 \sinh\left(\frac{\Xi_m x}{L}\right) + a_4 \sin\left(\frac{\Xi_m x}{L}\right)\right] \quad (26)$$

Table 1 shows the Ξ_m and Ω_m, and the a_i values ($i = 1, \ldots, 4$) from equations (23) and (24) for the three feasible combinations of boundary conditions.

Table 1. Boundary conditions and their associated Ξ_m, Ω_m, and a_i values.

B.C	a_i $(i = 1, \ldots, 4)$	Ξ_m	Ω_m
S-S	$a_1 = 0,\ a_2 = 0,$ $a_3 = 0,\ a_4 = -1,$	$m\pi$	1
C-S	$a_1 = 1,\ a_2 = -1,$ $a_3 = 1,\ a_4 = -1,$	$\frac{(4m+1)\pi}{4}$	$\frac{\cosh(\Xi_m) - \cos(\Xi_m)}{\sinh(\Xi_m) - \sin(\Xi_m)}$
C-C	$a_1 = 1,\ a_2 = -1,$ $a_3 = 1,\ a_4 = -1,$	$\frac{(2m+1)\pi}{2}$	$\frac{\cosh(\Xi_m) - \cos(\Xi_m)}{\sinh(\Xi_m) - \sin(\Xi_m)}$

The Galerkin procedure will be employed to construct a residual algebraic expression by replacing equation (25) into equations (B1-B9). The demonstration of the orthogonality between the residual and the test function systems may be presented as follows:

$$\iint R(x,y) X_m(x) Y_n(\theta) dx d\theta = 0, \quad m, n = 1,2,3, \ldots \quad (27)$$

Equilibrium equations may be represented by a matrix with the help of the formula given in relation (27), which is as

$$([\mathbf{M}]_{9\times9}\omega^2 - [\mathbf{K}]_{9\times9})\bar{\mathbf{q}} = 0, \quad (28)$$

where $\bar{\mathbf{q}} = \left(\bar{\bar{u}}, \bar{\bar{\psi}}_x, \bar{\bar{v}}, \bar{\bar{\psi}}_\theta, \bar{\bar{w}}, \bar{\bar{\Phi}}_{in}, \bar{\bar{\Phi}}_{ex}, \bar{\bar{\Psi}}_{in}, \bar{\bar{\Psi}}_{ex}\right)^T$, and the matrices $[\mathbf{K}]_{9\times9}$ and $[\mathbf{M}]_{9\times9}$ correspond to stiffness and mass characteristics, respectively. Finding a non-trivial solution to equation (28) yields the natural frequency of the sandwich FG microshell with internal and external MEE micro patches. In order to attain the frequency solutions, the determinant of the matrix appearing on the left-hand side of the characteristic equation is equated to zero.

4. Findings and discussion

It is important to note that the FG microshell consists of two unique materials, specifically Si_3N_4 and SUS304. Additionally, all internal and exterior MEE micro patches are composed of $BaTiO_3$-$CoFe_2O_4$ piezomagnetic material. The physical properties of these materials are subject to variations in temperature, as outlined in Table 2 and Table 3.

Table 2. Metal and ceramic properties in an FG microshell and their temperature dependency.

Material	Properties	G_0	G_{-1}	G_1	G_2	G_3
Metal (SUS304)	E(Pa)	201.04e+9	0	-3.079e-4	6.534e-7	-7.223e-10
	ρ(Kg/m^3)	8166	0	0	0	0
	ϑ	0.3262	0	-2.002e-4	3.797e-7	0
	k(W/mK)	15.379	0	-1.264e-3	2.092e-6	-7.223e-10
	α(1/K)	12.33e-6	0	8.086e-4	0	0
Ceramic (Si_3N_4)	E(Pa)	348.43e+9	0	-3.07e-4	2.16e-7	-8.946e-11
	ρ(Kg/m^3)	2370	0	0	0	0
	ϑ	0.24	0	0	0	0
	k(W/mK)	13.723	0	-1.032e-3	5.466e-7	-7.876e-11
	α(1/K)	5.8723e-6	0	9.095e-4	0	0

Table 3. Material properties of MEE micropatches.

Properties of MEE micropatch	$BaTiO_3 - CoFe_2O_4$
Elastic (GPa)	$\bar{c}_{11} = 226, \bar{c}_{12} = 125, \bar{c}_{22} = 226,$ $\bar{c}_{44} = 44.2, \bar{c}_{55} = 44.2, \bar{c}_{66} = 51$
Piezoelectric (C m^{-2})	$\bar{e}_{31} = -2.2, \bar{e}_{32} = -2.2,$ $\bar{e}_{24} = 5.8, \bar{e}_{15} = 5.8$
Dielectric (10^{-9}C V^{-1} m^{-1})	$\bar{\kappa}_{11} = 5.64, \quad \bar{\kappa}_{22} = 5.64,$ $\bar{\kappa}_{33} = 6.35$
Piezomagnetic (N A^{-1} m^{-1})	$\bar{q}_{31} = 290.1, \bar{q}_{32} = 290.1,$ $\bar{q}_{24} = 275, \bar{q}_{15} = 275$
Magnetoelectric (10^{-12}N S V^{-1} C^{-1})	$\bar{a}_{11} = 5.367, \bar{a}_{22} = 5.367,$ $\bar{a}_{33} = 2737.5$
Magnetic (10^{-6}N s^2 C^{-2})	$\bar{\mu}_{11} = -297, \quad \bar{\mu}_{22} = -297,$ $\bar{\mu}_{33} = 83.5$
Mass density (Kg m^{-3})	$\rho_m = 5550$
Thermal moduli (10^5N/K m^2)	$\bar{\lambda}_1 = 4.74, \quad \bar{\lambda}_2 = 4.53$

4.1 Model validation study

During the model validation process, a comprehensive assessment is carried out to verify the precision and dependability of the proposed methodology. In the first validation, without considering smart MEE patches, FGMs, and thermal effects, the non-dimensional natural frequencies ($\varpi = \omega R\sqrt{\frac{\rho_m}{E_m}}$) of a homogeneous cylindrical microshell ($m = 1, \frac{L}{R} = 1$) for simply supported boundary condition are obtained in terms of the circumferential wave number and thickness-to-radius ratio based on the derived relations and proposed solution technique in the present paper. The outcomes are compared with Ref. [69] in Table 4. This validation additionally takes into account the inclusion or exclusion of a length-scale parameter. The comparison depicted in Table 4 demonstrates a notable agreement between the conclusions derived from this investigation and the analytical estimations referenced.

Table 4. Validation of the dimensionless natural frequencies of a homogeneous cylindrical microshell against the length scale parameter.

h/R	n	Present		Ref. [69]	
		$l = 0$	$l = h$	$l = 0$	$l = h$
0.1	1	0.9339	1.1265	0.933	1.126
	2	0.7769	1.0675	0.776	1.0688
	3	0.7135	1.2072	0.713	1.207
0.2	1	1.0489	1.5373	1.048	1.537
	2	0.9710	1.5905	0.971	1.590
	3	1.0521	1.9281	1.052	1.928
0.3	1	1.1810	1.8780	1.181	1.878
	2	1.1629	1.9748	1.162	1.974
	3	1.3306	2.4156	1.330	2.415

In the next validation, without considering MEE patches and thermal effects, the non-dimensional frequencies ($\varpi = \omega R\sqrt{\frac{\rho_m}{E_m}}$) of a cylindrical microshell made of FGMs ($N = 1, \frac{L}{R} = 10, \frac{h}{R} = 0.05, m = 1$) are obtained for different boundary conditions based on the present model. The outcomes are compared with Ref. [73] in Table 5 in terms of the strain gradient parameter. The effectiveness and precision of the suggested approach in predicting the dimensionless natural frequency are demonstrated by its successful verification against the analytical data presented in Ref. [73]. In the final validation, without considering FGMs, thermal effects, and MSGT, the natural frequencies (GHz) of a MEE cylindrical shell ($\zeta = 2\pi, h_m = 1\text{nm}, \frac{L}{R} = 12, \frac{R}{h_m} = 50$) are obtained under different boundary conditions and circumferential wave numbers based on the present model. The results are compared with Ref. [74] in Table 6. This table shows that the present results correlate quite well with those found in the literature, proving that the proposed model is

capable of accurately forecasting the natural frequencies of smart cylindrical shells.

Table 5. Validation of the dimensionless natural frequencies of a cylindrical microshell made of FGMs for different boundary conditions.

BC	Study	$n=1$		$n=2$		$n=3$	
		$l=0$	$l=17.6\mu m$	$l=0$	$l=17.6\mu m$	$l=0$	$l=17.6\mu m$
SS	Present	0.1450	0.2059	0.1011	2.5861	0.2448	5.8873
	Ref. [73]	0.1457	0.2065	0.1011	2.5864	0.2448	5.8876
CS	Present	0.2091	0.3095	0.1179	2.5902	0.2470	5.8913
	Ref. [73]	0.2099	0.3098	0.1181	2.5909	0.2471	5.8915
CC	Present	0.2604	0.4162	0.1394	2.6088	0.2503	5.8986
	Ref. [73]	0.2603	0.4160	0.1392	2.6087	0.2503	5.8987

Table 6. Validation of the natural frequencies (GHz) of a MEE cylindrical shell for different boundary conditions.

BC	Study	$n=1$	$n=2$	$n=3$	$n=4$
SS	Present	0.7185	0.4099	0.8000	1.4791
	Ref. [74]	0.7188	0.4101	0.8003	1.4793
CS	Present	0.9862	0.4906	0.8118	1.4819
	Ref. [74]	0.9863	0.4907	0.8121	1.4821
CC	Present	1.2628	0.6014	0.8314	1.4860
	Ref. [74]	1.2629	0.6014	0.8315	1.4863

4.2 Parametric study

Numerical simulations provide a helpful means to explore and understand the natural frequencies of microshells made of temperature-dependent FGMs and enhanced with micro patches made of MEE materials.

In Fig. 2, the effects of the dimensionless length scale parameter (l/h, $l=l_0=l_1=l_2$) and different boundary conditions on the changes in the natural frequency of an FG microshell with embedded internal and external MEE micropatches are investigated for three different theories, including the CCT when $l_0=l_1=l_2=0$, the MCST when $l_0=l_1=0, l_2\neq 0$, and the MSGT when $l_0=l_1=l_2\neq 0$. For this case, let's assume that $h=1\mu m, h_m=0.5\mu m$, $R=50h, L=12R, T_t=300K, T_b=300K, N=1$, $Q=2$, $\zeta=15^\circ, m=1, n=1$, $V_0=0$, $\Gamma_0=0, K_W=0, K_G=0$. The findings indicate that the implementation of the clamped boundary condition leads to a higher natural frequency as compared to the utilization of the simply supported boundary condition. The clamped boundary condition imposes restrictions on both the translational and rotational degrees of freedom at the supports of the microshell. The present condition offers a higher level of constraint in comparison to the condition of simply supported, which just limits the translation perpendicular to the boundary. The findings indicate that the changes in frequency for the CCT remain consistent across varied values of the length scale parameter due to the absence of this parameter in the theory. The length scale parameter serves to quantify the impact of size effects observed at microscales. An increase in the value of this parameter leads to a corresponding rise in strain energy, resulting in elevated stiffness and natural frequency. As was previously established, a rise in this parameter results in greater stiffness and natural frequency due to a larger strain energy density. Moreover, the presence of rotation gradients in the MSGT also plays a role in augmenting stiffness as compared to the mere inclusion of couple stresses in the MCST. It is also shown that the length scale parameter has a more noticeable impact on the frequency variations for the simply supported boundary condition.

In Fig. 3, the effects of the power-law index parameter, which represents the percentage of ceramic or metal in the FG core, on the vibrations of the sandwich microshell are shown for different boundary conditions when $h=1\mu m, h_m=0.5\mu m$, $R=50h, L=12R, T_t=300K, T_b=300K$, $Q=2$, $\zeta=15^\circ, m=1, n=1$, $V_0=0$, $\Gamma_0=0$, $l_0=l_1=l_2=0$, $K_W=0, K_G=0$. As can be seen, with increasing power-law index parameters, the natural frequency of the system (initially sharply and then gradually) decreases. A higher value of this index corresponds to a greater metallic volume fraction compared to ceramic. Metals exhibit a lower modulus of elasticity compared to ceramics. As the power-law index grows, there is a change in the composition from being mostly ceramic to predominantly metal. Initially, the frequency drops sharply because the composition changes rapidly from ceramic to metal. Later, the composition variation becomes more gradual, leading to a more mild decrease in frequency.

The influences of the circumferential and axial wave numbers on the changes in natural frequency of the system are shown in Fig. 4 when $h=1\mu m, h_m=0.5\mu m$, $R=50h, L=12R, T_t=300K, T_b=300K$, $Q=2$, $\zeta=15^\circ, N=1, V_0=0$, $\Gamma_0=0$, $l_0=l_1=l_2=0, K_W=0, K_G=0$. By closely observing the figure, it is evident that the natural frequency of the microshell in the second circumferential mode is lower than the first circumferential mode, and then from the third circumferential mode onwards, the natural frequency increases. It is also observed that at higher circumferential modes above 4 ($n\geq 4$), the effects of the axial mode on the natural frequency become negligible. The second circumferential mode shape is more flexible and exhibits

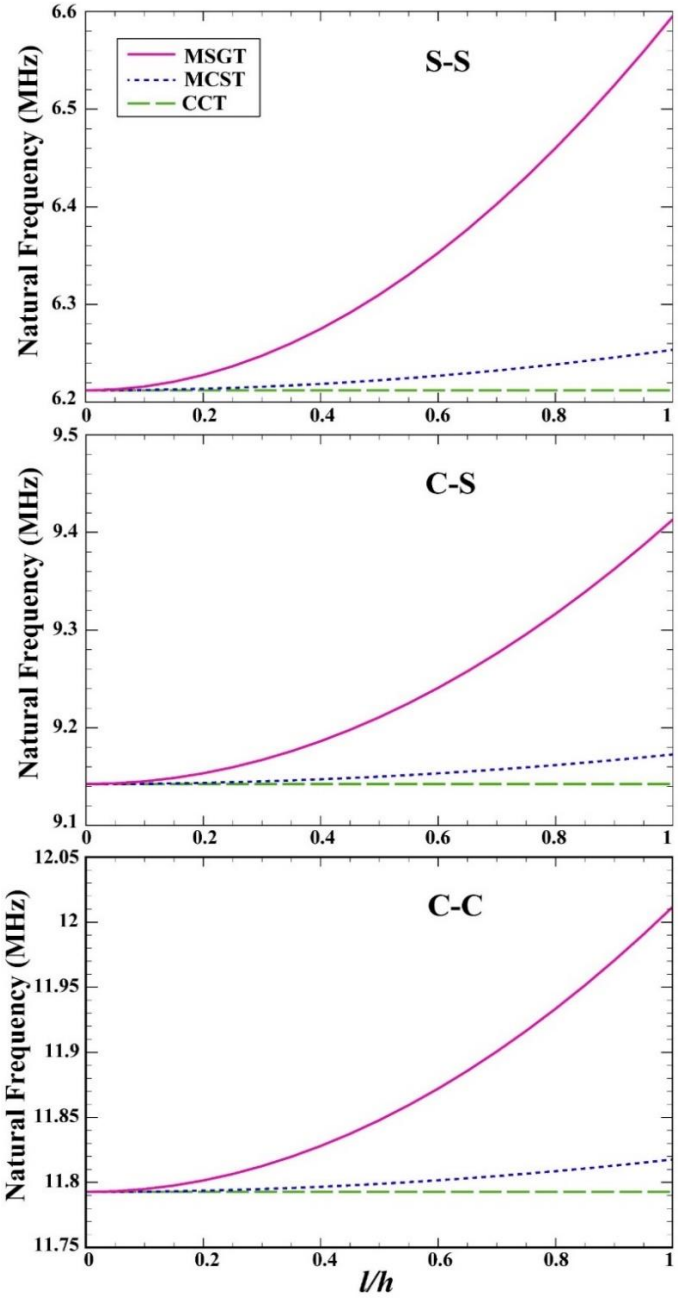

Fig. 2 Effects of length scale parameter and boundary conditions on natural frequency changes of an FG microshell with embedded internal and external MEE micro patches for different theories.

greater curvature than the first mode. More flexible modes have lower frequencies. The localization of higher circumferential modes results in higher constraints and stiffness. Moreover, in the case of greater circumferential modes, the dominant factor influencing the vibrations is the circumferential deformations rather than the axial deformations. At this point, circumferential stiffness assumes a dominant role.

The investigation presented in Fig. 5 examines the impact of the number of MEE patches on the vibrational characteristics of the sandwich microshell under varying boundary conditions and length scale parameters when $h = 1\mu\text{m}, h_m = 0.5\mu\text{m},\ R = 50h, L = 12R, T_t = 300\text{K}, T_b = 300\text{K},\ N = 1,\ \zeta = 15^{\circ}, m = 1, n = 1,\ V_0 = 0,\ \Gamma_0 = 0,\ K_{\text{W}} = 0, K_{\text{G}} = 0$. By closely observing this figure, it can be seen that by increasing the number of MEE patches, the natural frequency of the structure decreases. The MEE micropatches induce additional flexibility in the system compared to the base microshell. More patches lead to higher overall flexibility. Additionally, more patches increase the effective mass of the system. Higher mass leads to lower natural frequencies.

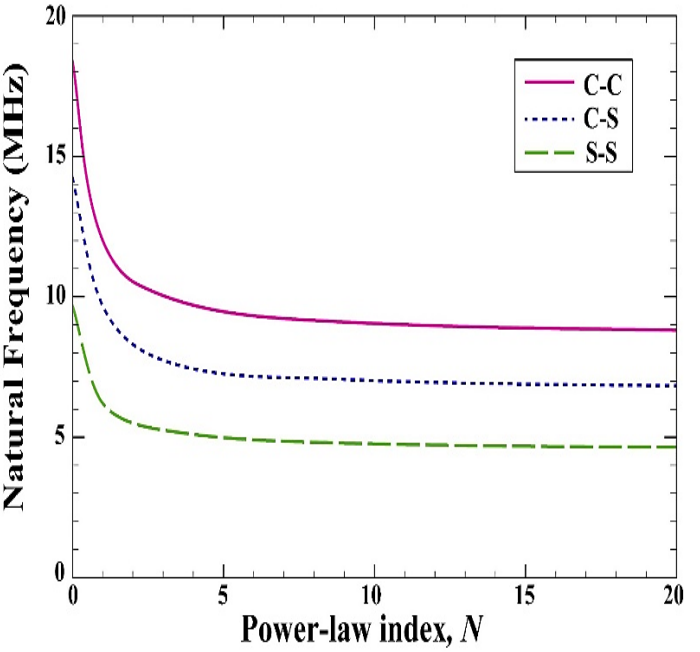

Fig. 3 Effects of power-law index parameter on natural frequency under various boundary conditions.

Figure 6 displays the effect of the angular pitch of MEE patches on the vibrational characteristics of the sandwich microshell under varying boundary conditions and length scale parameters when $h = 1\mu\text{m}, h_m = 0.5\mu\text{m},\ R = 50h, L = 12R, T_t = 300\text{K}, T_b = 300\text{K},\ N = 1,\ Q = 2, m = 1, n = 1,\ V_0 = 0,\ \Gamma_0 = 0, K_{\text{W}} = 0, K_{\text{G}} = 0$. As seen in Fig. 6, it is worth mentioning that the fundamental frequency of the system decreases as the angular pitch of the MEE patches increases. The potential explanation for this phenomenon may be analogous to the impact of the number of patches on the natural frequency. Increasing the angular pitch means the patches are spaced farther apart circumferentially on the shell surface. Therefore, the increased spacing and discontinuity from a larger angular pitch reduce stiffness, resulting in decreased natural frequencies.

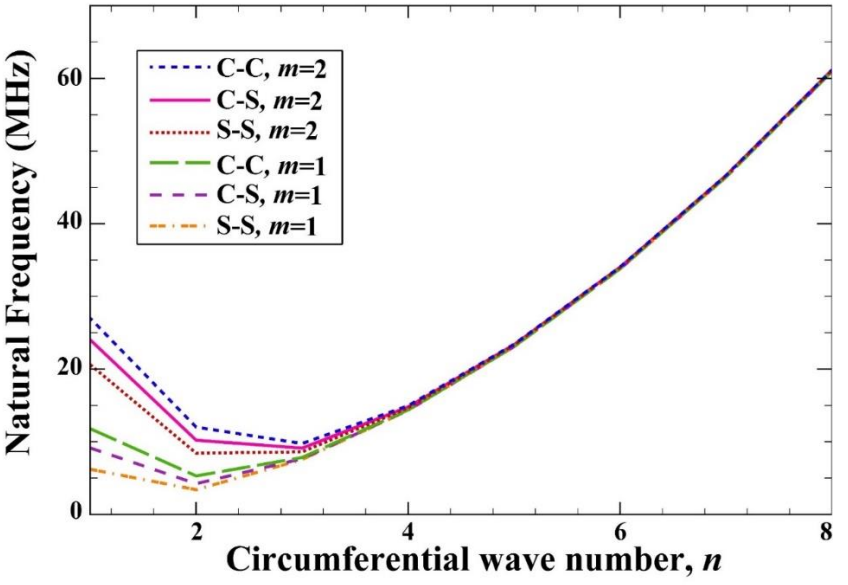

Fig. 4 Effects of axial and circumferential wave numbers on natural frequency changes under different boundary conditions.

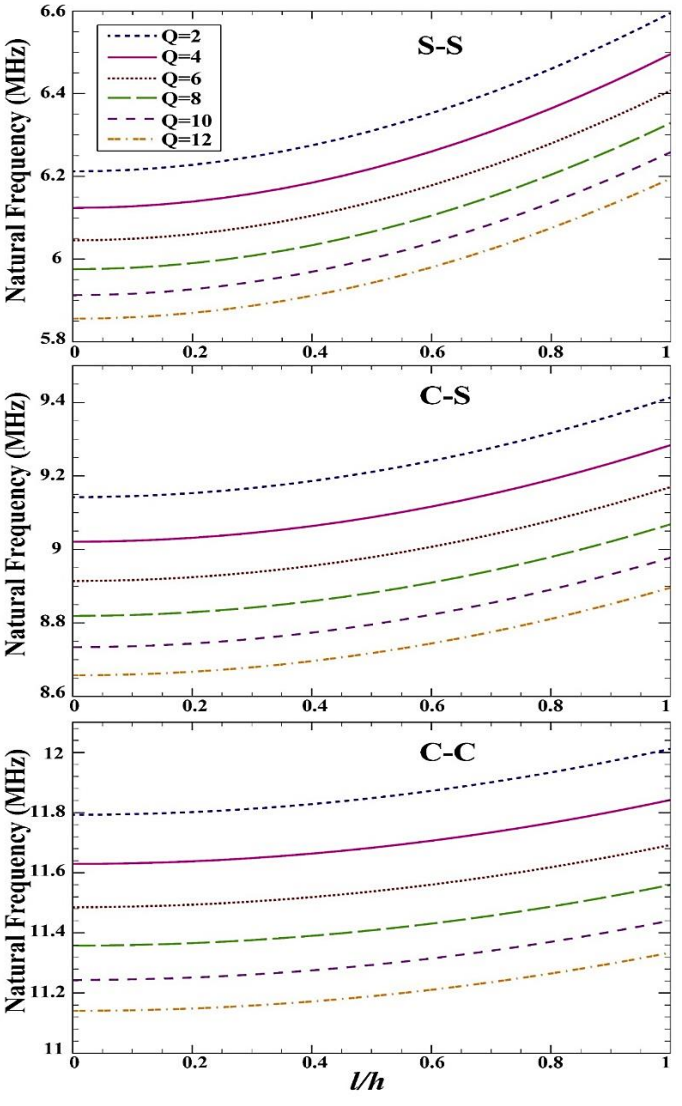

Fig. 5 Effect of the number of MEE patches on the vibrational characteristics of the sandwich microshell.

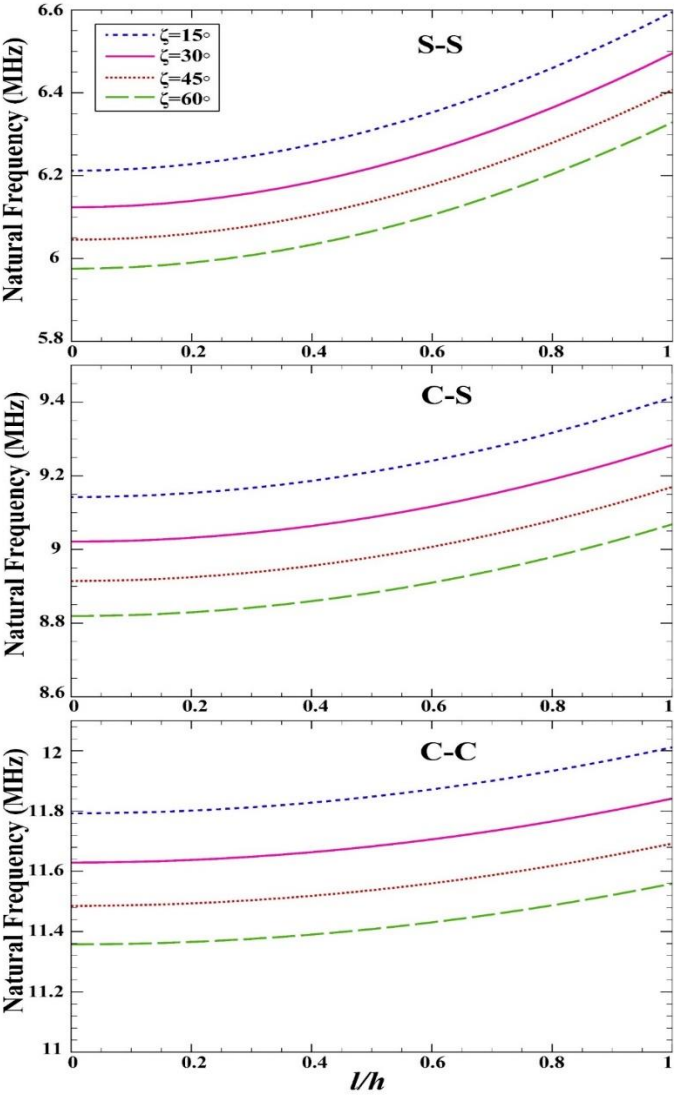

Fig. 6 Effect of angular pitch of MEE patches on the natural frequency of the sandwich microshell.

Figure 7 presents the effects of the temperature and different temperature profiles on the changes of the natural frequency for different boundary conditions when $h = 1\mu m, h_m = 0.5\mu m,\ R = 50h, L = 12R, Q = 2,\ N = 1,\ \zeta = 15^{\circ}, m = 1, n = 1,\ V_0 = 0,\ \Gamma_0 = 0, K_W = 0, K_G = 0$. According to the findings, it can be observed that the natural frequency of the system drops as the temperature increases for all three temperature distribution profiles. Temperature-dependent materials, such as functionally graded shells, experience compositional changes and property degradation at elevated temperatures, leading to a reduction in stiffness. In addition, it should be noted that thermal expansions occurring at higher temperatures result in enhanced flexibility and decreased natural frequencies. Moreover, the findings indicate that the effect of temperature changes on the vibrational characteristics of the structure is more pronounced when considering a UDT profile compared to the HTR and NTD patterns. The UDT profile applies uniformly increased temperature to the whole structure. This phenomenon leads to extensive material softening and degradation. In contrast, the NTD and HTR profiles involve localized or gradual heating. Parts of the structure retain higher stiffness.

In Fig. 8, the effects of electric voltage (V_0) and the thickness ratio $\left(\frac{h_m}{h}\right)$ of the MEE patch to the FG core on the natural frequency of the structure are evaluated for simply supported boundary conditions when $h = 1\mu m, h_m = 0.5\mu m, R = 50h, L = 12R, T_t = 300K, T_b = 300K,\ N = 1,\ \zeta = 15^{\circ}, m = 1, n = 1,\ Q = 2,\ \Gamma_0 = 0, K_W = 0, K_G = 0$. It is observed that with increasing electric voltage, the natural frequency of the structure decreases. At the physiological level, the application of positive and negative electric voltage to the MEE patches results in the generation of axial and circumferential forces. The compressive and tensile pressures exerted on the charged atoms and molecules result in their displacement in different directions. Additional strain is produced in the MEE patches as a result of the charged particles' physical deformation and displacement from their equilibrium locations under the effect of the electric voltage. The interatomic connections undergo stretching and compression, resulting in increased material flexibility. This disrupts the atomic bonds and reduces stiffness. It is also observed that with an increasing thickness ratio of the MEE patch to the FG core, the natural frequency reduces due to the reduction in structural stiffness.

In Fig. 9, for simply supported boundary conditions, the influences of magnetic potential (Γ_0) and the ratio of shell length to its radius $(\frac{L}{R})$ on the natural frequency are investigated when $h = 1\mu m, h_m = 0.5\mu m,\ R = 50h, L = 12R, T_t = 300K, T_b = 300K,\ N = 1,\ \zeta = 15^{\circ}, m = 1, n = 1,\ Q = 2,\ V_0 = 0, K_W = 0, K_G = 0$. The findings indicate that when the magnetic potential increases, there is a corresponding increase in the natural frequency of the structure. The application of positive or negative magnetic potential induces axial forces inside the MEE patch. A positive magnetic potential gives rise to an axial force that is tensile in nature, whereas a negative magnetic potential generates a compressive force along the axis. These axial

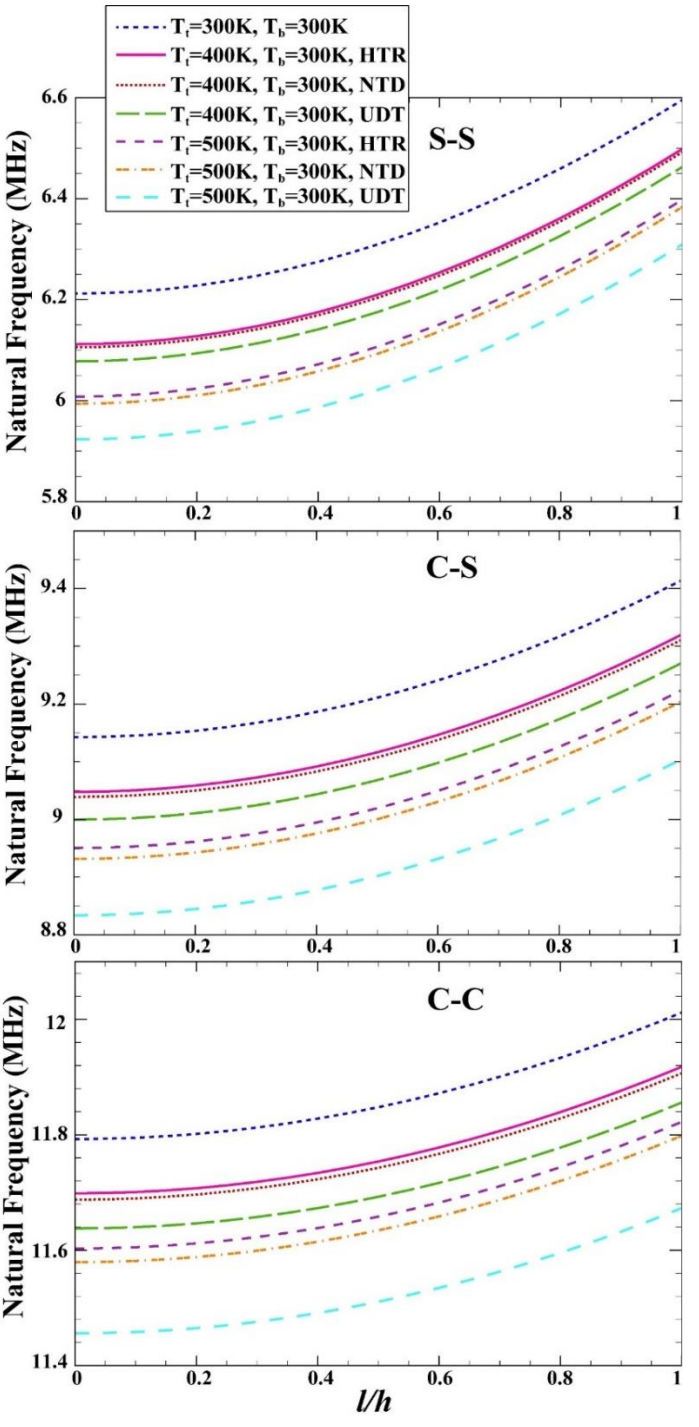

Fig. 7 Effects of the temperature and different temperature profiles on the changes of the natural frequency.

forces act to stiffen the MEE patch in the axial direction. Hence, a greater degree of stiffness results in an augmented natural frequency. Additionally, the results indicate that with an increasing ratio of shell length to radius, the natural frequency decreases.

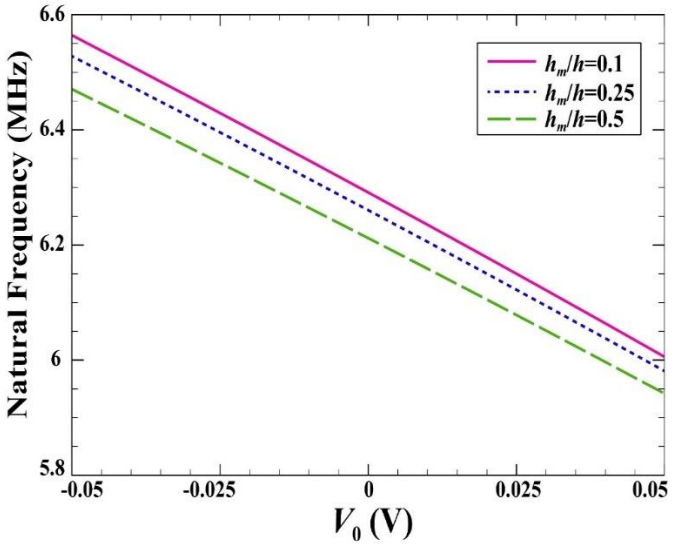

Fig. 8 Effects of electric voltage (V_0) and the thickness ratio $\left(\frac{h_m}{h}\right)$ on the natural frequency.

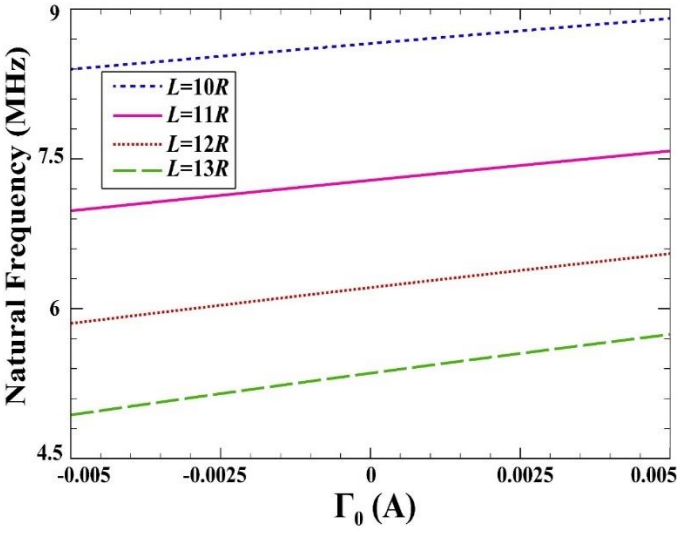

Fig. 9 Effects of magnetic potential (Γ_0) and the ratio of shell length to its radius $\left(\frac{L}{R}\right)$ on the natural frequency.

Finally, for simply supported boundary conditions, the influences of Winkler and shear stiffnesses of Pasternak medium on the natural frequency of the system are presented in Fig. 10 when $h = 1\mu m, h_m = 0.5\mu m$, $R = 50h, L = 12R, T_t = 300K, T_b = 300K$, $N = 1$, $\zeta = 15^{\circ}, m = 1, n = 1$, $Q = 2$, $V_0 = 0, \Gamma_0 = 0$. The figure illustrates a positive correlation between the shear stiffness and Winkler parameters of the Pasternak foundation and the natural frequency of the system. To summarize, a foundation with increased stiffness exhibits more resistance to vibration, leading to an elevated natural frequency for the structural system.

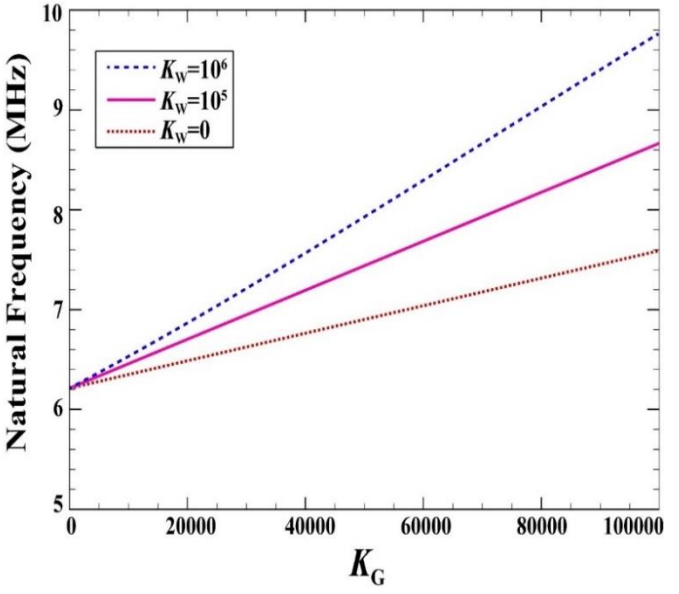

Fig. 10 Effects of Winkler and shear stiffnesses of Pasternak medium on the natural frequency.

5. Conclusions

This study presented a comprehensive theoretical framework to evaluate the free vibrations of FG microshells with MEE micro patches under temperature-dependent properties. The FSDT accurately captured structural responses. The MSGT incorporated size effects through length-scale parameters. Three temperature profiles were considered across the microshell thickness. The material properties of the graded core followed a power-law distribution and varied with temperature. Hamilton's principle derived the coupled equations, which were solved using Galerkin's technique to obtain natural frequencies. Comparative results validated the accuracy of the proposed model. A thorough parametric analysis provided critical insights into the influence of gradient index, length scales, temperature variation, patch characteristics, Pasternak medium's parameters, electric voltage, and magnetic potential on free vibration performance. This study elucidated the capabilities of integrated patches in modulating the dynamic behavior of temperature-dependent FG microshells. The results delivered valuable knowledge to optimize the design of microscale sensors and actuators. Key findings that emerged from this research include:

- The larger angular pitch of MEE patches decreases natural frequency owing to increased spacing and discontinuity.
- Increasing the number of MEE patches reduces natural

frequency due to higher flexibility.

- Natural frequency drops more significantly for uniform temperature distributions compared to nonlinear and harmonic profiles.
- Increasing electric voltage decreases natural frequency due to atomic bond weakening and higher flexibility.
- Augmented magnetic potential increases natural frequency by inducing axial stiffening forces in patches.

While this study provides a solid foundation, further research can build upon these findings in several directions. Future studies could investigate the dynamic buckling and nonlinear vibration of FG-MEE cylindrical microshells using this framework. The vibration control and active tuning of these structures through integrated MEE patches present another promising area for future exploration. Experiments on FG-MEE microshell prototypes could validate the theoretical predictions and provide further insights. Extending the current approach to analyze other boundary conditions and geometries, such as spherical or conical microshells, could also be worthwhile.

Acknowledgements

This study was supported by Thammasat Postdoctoral Fellowship, Thammasat University Research Division, Thammasat University.

Conflict of Interest

There is no conflict of interest.

Supporting Information

Applicable. Appendix A and B is available and uploaded in separate file.

References

[1] M. Amabili, M. P. Paı̈doussis, Review of studies on geometrically nonlinear vibrations and dynamics of circular cylindrical shells and panels, with and without fluid-structure interaction, *Applied Mechanics Reviews*, 2003, **56**, 349-381, doi: 10.1115/1.1565084.

[2] S. M. Fatemi, H. Showkati, M. Maali, Experiments on imperfect cylindrical shells under uniform external pressure, *Thin-Walled Structures*, 2013, **65**, 14-25, doi: 10.1016/j.tws.2013.01.004.

[3] M. R. Ahmad Fuaad, M. N. Hasan, M. I. Ahmad Asri, M. S. Mohamed Ali, Microactuators technologies for biomedical applications, *Microsystem Technologies*, 2023, **29**, 953-984, doi: 10.1007/s00542-023-05489-8.

[4] A. C. Eringen, D. G. B. Edelen, On nonlocal elasticity, *International Journal of Engineering Science*, 1972, **10**, 233-248, doi: 10.1016/0020-7225(72)90039-0.

[5] A. C. Eringen, Linear theory of nonlocal elasticity and dispersion of plane waves, *International Journal of Engineering Science*, 1972, **10**, 425-435, doi: 10.1016/0020-7225(72)90050-x.

[6] D. C. C. Lam, F. Yang, A. C. M. Chong, J. Wang, P. Tong, Experiments and theory in strain gradient elasticity, *Journal of the Mechanics and Physics of Solids*, 2003, **51**, 1477-1508, doi: 10.1016/s0022-5096(03)00053-x.

[7] R. D. Mindlin. Microstructure in linear elasticity. Columbia univ new york dept of civil engineering and engineering mechanics, 1963.

[8] F. Yang, A. C. M. Chong, D. C. C. Lam, P. Tong, Couple stress based strain gradient theory for elasticity, *International Journal of Solids and Structures*, 2002, **39**, 2731-2743, doi: 10.1016/s0020-7683(02)00152-x.

[9] C. W. Lim, G. Zhang, J. N. Reddy, A higher-order nonlocal elasticity and strain gradient theory and its applications in wave propagation, *Journal of the Mechanics and Physics of Solids*, 2015, **78**, 298-313, doi: 10.1016/j.jmps.2015.02.001.

[10] M. Hosseini, M. Bahreman, A. Jamalpoor, Thermomechanical vibration analysis of FGM viscoelastic multi-nanoplate system incorporating the surface effects via nonlocal elasticity theory, *Microsystem Technologies*, 2017, **23**, 3041-3058, doi: 10.1007/s00542-016-3133-7.

[11] A. Kiani, M. Sheikhkhoshkar, A. Jamalpoor, M. Khanzadi, Free vibration problem of embedded magneto-electro-thermo-elastic nanoplate made of functionally graded materials via nonlocal third-order shear deformation theory, *Journal of Intelligent Material Systems and Structures*, 2018, **29**, 741-763, doi: 10.1177/1045389x17721034.

[12] E. Salari, A. Ashoori, S. A. S. Vanini, Porosity-dependent asymmetric thermal buckling of inhomogeneous annular nanoplates resting on elastic substrate, *Advances in Nano Research*, 2019, **7**, 25, doi: 10.12989/anr.2019.7.1.025.

[13] F. Ebrahimi, E. Salari, Thermal loading effects on electro-mechanical vibration behavior of piezoelectrically actuated inhomogeneous size-dependent Timoshenko nanobeams, *Advances in Nano Research*, 2016, **4**, 197-228, doi: 10.12989/anr.2016.4.3.197.

[14] E. Salari, S. A. Sadough Vanini, Small/large amplitude vibration, snap-through and nonlinear thermo-mechanical instability of temperature-dependent FG porous circular nanoplates, *Engineering with Computers*, 2023, **39**, 2295-2326, doi: 10.1007/s00366-022-01629-2.

[15] J. Ehyaei, F. Ebrahimi, E. Salari, Nonlocal vibration analysis of FG nano beams with different boundary conditions, *Advances in Nano Research*, 2016, **4**, 85-111, doi: 10.12989/anr.2016.4.2.085.

[16] L. Bo, Nonlinear dynamic analysis of the perovskite solar cell under blast impacts based on the modified strain gradient theory, *Acta Mechanica*, 2023, **234**, 1649-1685, doi: 10.1007/s00707-022-03444-8.

[17] L. Yang, P. Li, Q. Gao, T. Gao, Thermoelastic damping in rectangular micro/nanoplate resonators by considering three-dimensional heat conduction and modified couple stress theory,

Journal of Thermal Stresses, 2022, **45**, 843-864, doi: 10.1080/01495739.2022.2103058.
[18] P. R. Saffari, S. O. Ismail, C. Thongchom, S. Sirimontree, T. Jearsiripongkul, Effect of magnetic field on vibration of electrorheological fluid nanoplates with FG-CNTRC layers, *Journal of Vibration Engineering & Technologies*, 2023, 1-20, doi: 10.1007/s42417-023-01048-7.
[19] C. Thongchom, P. Roodgar Saffari, P. Roudgar Saffari, N. Refahati, S. Sirimontree, S. Keawsawasvong, S. Titotto, Dynamic response of fluid-conveying hybrid smart carbon nanotubes considering slip boundary conditions under a moving nanoparticle, *Mechanics of Advanced Materials and Structures*, 2023, **30**, 2135-2148, doi: 10.1080/15376494.2022.2051101.
[20] Y. Zarabimanesh, P. Roodgar Saffari, P. Roudgar Saffari, N. Refahati, Hygro-thermo-mechanical vibration of two vertically aligned single-walled boron nitride nanotubes conveying fluid, *Journal of Vibration and Control*, 2022, **28**, 2101-2120, doi: 10.1177/10775463211006512.
[21] R. Ansari, R. Gholami, S. Ajori, Torsional vibration analysis of carbon nanotubes based on the strain gradient theory and molecular dynamic simulations, *Journal of Vibration and Acoustics*, 2013, **135**, 051016, doi: 10.1115/1.4024208.
[22] Z. K. Mizuji, M. Ghadiri, A. Rajabpour, M. F. Ahari, A. Zajkani, S. Yazdinia, Numerical modeling of a body vessel for dynamic study of a nano cylindrical shell carrying fluid and a moving nanoparticle, *Engineering Analysis with Boundary Elements*, 2023, **152**, 362-382, doi: 10.1016/j.enganabound.2023.04.005.
[23] S.-H. Chi, Y.-L. Chung, Mechanical behavior of functionally graded material plates under transverse load—part II: numerical results, *International Journal of Solids and Structures*, 2006, **43**, 3675-3691, doi: 10.1016/j.ijsolstr.2005.04.010.
[24] P. R. Saffari, S. Sirimontree, C. Thongchom, T. Jearsiripongkul, P. R. Saffari, S. Keawsawasvong, S. Kongwat, Free and forced vibration of sandwich FGM porous variable thickness nanoplates integrated with magneto-electro-elastic layers via nonlocal strain gradient theory, *Engineered Science*, 2023, **24**, 918, doi: 10.30919/es918.
[25] A. Tounsi, A. A. Bousahla, S. I. Tahir, A. H. Mostefa, F. Bourada, M. A. Al-Osta, A. Tounsi, Influences of different boundary conditions and hygro-thermal environment on the free vibration responses of FGM sandwich plates resting on viscoelastic foundation, *International Journal of Structural Stability and Dynamics*, 2023, doi: 10.1142/s0219455424501177.
[26] A. Tounsi, A. H. Mostefa, A. Attia, A. A. Bousahla, F. Bourada, A. Tounsi, M. A. Al-Osta, Free vibration investigation of functionally graded plates with temperature dependent properties resting on a viscoelastic foundation, *Structural Engineering and Mechanics*, 2023, **86**, 1-16, doi: 10.12989/sem.2023.86.1.001.
[27] A. Tounsi, S. I. Tahir, M.A. Al-Osta, T. Do-Van, F. Bourada, A. A. Bousahla, A. Tounsi, An integral quasi-3D computational model for the hygro-thermal wave propagation of imperfect FGM sandwich plates, *Computers and Concrete*, 2023, **32**, 61-74, doi: 10.12989/cac.2023.32.1.061.
[28] F. Bounouara, M. Sadoun, M. M. Selim Saleh, A. Chikh, A. A. Bousahla, A. Kaci, F. Bourada, A. Tounsi, A. Tounsi, Effect of visco-Pasternak foundation on thermo-mechanical bending response of anisotropic thick laminated composite plates, *Steel and Composite Structures*, 2023, **47**, 693-707, doi: 10.12989/scs.2023.47.6.693.
[29] C. Thongchom, T. Jearsiripongkul, N. Refahati, P. Roudgar Saffari, P. Roodgar Saffari, S. Sirimontree, S. Keawsawasvong, Sound transmission loss of a honeycomb sandwich cylindrical shell with functionally graded porous layers, *Buildings*, 2022, **12**, 151, doi: 10.3390/buildings12020151.
[30] C. Thongchom, P. R. Saffari, N. Refahati, P. R. Saffari, H. Pourbashash, S. Sirimontree, S. Keawsawasvong, An analytical study of sound transmission loss of functionally graded sandwich cylindrical nanoshell integrated with piezoelectric layers, *Scientific Reports*, 2022, **12**, 3048, doi: 10.1038/s41598-022-06905-1.
[31] E. Salari, S. A. Sadough Vanini, Nonlocal nonlinear static/dynamic snap-through buckling and vibration of thermally post-buckled imperfect functionally graded circular nanoplates, *Waves in Random and Complex Media*, 2022, 1-47, doi: 10.1080/17455030.2022.2055810.
[32] E. Salari, A. R. Ashoori, S. A. Sadough Vanini, A. H. Akbarzadeh, Nonlinear dynamic buckling and vibration of thermally post-buckled temperature-dependent FG porous nanobeams based on the nonlocal theory, *Physica Scripta*, 2022, **97**, 085216, doi: 10.1088/1402-4896/ac8187.
[33] E. Heydari, A. Mokhtarian, M. Pirmoradian, M. Hashemian, A. Seifzadeh, Acoustic wave transmission of double-walled functionally graded cylindrical microshells under linear and nonlinear temperature distributions using modified strain gradient theory, *Thin-Walled Structures*, 2021, **169**, 108430, doi: 10.1016/j.tws.2021.108430.
[34] T. M. Le, D. Vo, Z. Y. Aung, E. Atroshchenko, T. Q. Bui, J. Rungamornrat, Isogeometric analysis of shear-deformable, in-plane functionally graded microshells by Mindlin's strain gradient theory, *Engineering with Computers*, 2023, 1-34, doi: 10.1007/s00366-023-01821-y.
[35] Z. Lyu, W. Liu, C. Liu, Y. Zhang, M. Fang, Thermo-electro-mechanical vibration and buckling analysis of a functionally graded piezoelectric porous cylindrical microshell, *Journal of Mechanical Science and Technology*, 2021, **35**, 4655-4672, doi: 10.1007/s12206-021-0933-1.
[36] G. Zhao, M. Hooman, M. Yarigarravesh, M. Algarni, M. Jade Catalan Opulencia, F. Alsaikhan, A. Turki Jalil, A. Mohamed, K. M.Aboras, M. L. Rahman, M. Sani Sarjadi, Vibration analysis of size dependent micro FML cylindrical shell reinforced by CNTs based on modified couple stress theory, *Arabian Journal of Chemistry*, 2022, **15**, 104115, doi: 10.1016/j.arabjc.2022.104115.
[37] M. Taghizadeh, M. Babaei, R. Dimitri, F. Tornabene, Assessment of critical buckling load of bi-directional functionally graded truncated conical micro-shells using modified couple stress theory and Ritz method, *Mechanics Based Design of Structures and Machines*, 2023, 1-32, doi: 10.1080/15397734.2023.2202230.

[38] I. M. Mudhaffar, A. Chikh, A. Tounsi, M. A. Al-Osta, M. M. Al-Zahrani, S. U. Al-Dulaijan, Impact of viscoelastic foundation on bending behavior of FG plate subjected to hygro-thermo-mechanical loads, *Structural Engineering and Mechanics*, 2023, **86**, 167-180, doi: 10.12989/sem.2023.86.2.167.
[39] M. W. Zaitoun, A. Chikh, A. Tounsi, A. Sharif, M. A. Al-Osta, S. U. Al-Dulaijan, M. M. Al-Zahrani, An efficient computational model for vibration behavior of a functionally graded sandwich plate in a hygrothermal environment with viscoelastic foundation effects, *Engineering with Computers*, 2023, **39**, 1127-1141, doi: 10.1007/s00366-021-01498-1.
[40] M. W. Zaitoun, A. Chikh, A. Tounsi, M. A. Al-Osta, A. Sharif, S. U. Al-Dulaijan, M. M. Al-Zahrani, Influence of the visco-Pasternak foundation parameters on the buckling behavior of a sandwich functional graded ceramic–metal plate in a hygrothermal environment, *Thin-Walled Structures*, 2022, **170**, 108549, doi: 10.1016/j.tws.2021.108549.
[41] I. M. Mudhaffar, A. Tounsi, A. Chikh, M. A. Al-Osta, M. M. Al-Zahrani, S. U. Al-Dulaijan, Hygro-thermo-mechanical bending behavior of advanced functionally graded ceramic metal plate resting on a viscoelastic foundation, *Structures*, 2021, **33**, 2177-2189, doi: 10.1016/j.istruc.2021.05.090.
[42] M. Al-Osta, H. Saidi, A. Tounsi, S. Al-Dulaijan, M. Al-Zahrani, A. Sharif, A. Tounsi, Influence of porosity on the hygro-thermo-mechanical bending response of an AFG ceramic-metal plates using an integral plate model, *Smart Structures and Systems*, 2021, **28**, 499, doi: 10.12989/SSS.2021.28.4.499.
[43] B. Merazka, Bouhadra A., Menasria A., Selim M., A. Bousahla A., Bourada F., Tounsi A., H. Benrahou K., Tounsi A., Al-Zahrani M, Hygro-thermo-mechanical bending response of FG platesresting on elastic foundations, *Steel and Composite Structures*, 2021, **39**, 631, doi: 10.12989/SCS.2021.39.5.631.
[44] H. Bellifa, Selim M., A. Chikh, Chikh A., A. Bousahla A., Bourada F., Tounsi A., H. Benrahou K., Al-Zahrani M., Tounsi A, Influence of porosity on thermal buckling behavior of functionally graded beams, *Smart Structures and Systems*, 2021, **27**, 719-728, doi: 10.12989/sss.2021.27.4.719.
[45] M. Abualnour, A. Chikh, Chikh A., Hebali H., K. A., Tounsi A., A. Bousahla A., Tounsi A, Thermomechanical analysis of antisymmetric laminated reinforced composite plates using a new four variable trigonometric refined plate theory, *Computers and Concrete*, 2019, **24**, 489-498, doi: 10.12989/cac.2019.24.6.489.
[46] M. Hosseini, A. Jamalpoor, M. Bahreman, Small-scale effects on the free vibrational behavior of embedded viscoelastic double-nanoplate-systems under thermal environment, *Acta Astronautica*, 2016, **129**, 400-409, doi: 10.1016/j.actaastro.2016.10.001.
[47] M. Hosseini, A. Jamalpoor, Analytical solution for thermomechanical vibration of double-viscoelastic nanoplate-systems made of functionally graded materials, *Journal of Thermal Stresses*, 2015, **38**, 1428-1456, doi: 10.1080/01495739.2015.1073986.
[48] P. R. Saffari, C. Thongchom, T. Jearsiripongkul, P. R. Saffari, S. Keawsawasvong, S. Kongwat, Porosity-dependent wave propagation in multi-directional functionally graded nanoplate with nonlinear temperature-dependent characteristics on Kerr-type substrate, *International Journal of Thermofluids*, 2023, **20**, 100408, doi: 10.1016/j.ijft.2023.100408.
[49] A. H. Rajabi, M. Jaffe, T. L. Arinzeh, Piezoelectric materials for tissue regeneration: a review, *Acta Biomaterialia*, 2015, **24**, 12-23, doi: 10.1016/j.actbio.2015.07.010.
[50] Z. Deng, M. J. Dapino, Review of magnetostrictive materials for structural vibration control, *Smart Materials and Structures*, 2018, **27**, 113001, doi: 10.1088/1361-665x/aadff5.
[51] D. Rashadfar, B. Wooten, J. Heremans, Electric field dependent thermal conductivity on ferroelectrics and beyond: Study on polarization waves in electrostrictive materials, *The Bulletin of the American Physical Society*, 2023.
[52] C. Othmani, H. Zhang, C. Lü, Y. Q. Wang, A. Reza Kamali, Orthogonal polynomial methods for modeling elastodynamic wave propagation in elastic, piezoelectric and magneto-electro-elastic composites—a review, *Composite Structures*, 2022, **286**, 115245, doi: 10.1016/j.compstruct.2022.115245.
[53] S. Zhu, H. Yu, L. Hao, C. Huang, Z. Shen, J. Wang, L. Guo, Influences of magneto-electro-elastic layer properties of piezoelectric/piezomagnetic composites on dynamic intensity factors, *Applied Mathematical Modelling*, 2023, **120**, 535-557, doi: 10.1016/j.apm.2023.03.035.
[54] A. Jamalpoor, A. Ahmadi-Savadkoohi, M. Hosseini, S. Hosseini-Hashemi, Free vibration and biaxial buckling analysis of double magneto-electro-elastic nanoplate-systems coupled by a visco- Pasternak medium via nonlocal elasticity theory, *European Journal of Mechanics - A/Solids*, 2017, **63**, 84-98, doi: 10.1016/j.euromechsol.2016.12.002.
[55] M. Hosseini, M. R. Mofidi, A. Jamalpoor, M. Safi Jahanshahi, Nanoscale mass nanosensor based on the vibration analysis of embedded magneto-electro-elastic nanoplate made of FGMs via nonlocal Mindlin plate theory, *Microsystem Technologies*, 2018, **24**, 2295-2316, doi: 10.1007/s00542-017-3654-8.
[56] A. Jamalpoor, A. Ahmadi-Savadkoohi, S. Hosseini-Hashemi, Free vibration and biaxial buckling analysis of magneto-electro-elastic microplate resting on visco-Pasternak substrate via modified strain gradient theory, *Smart Materials and Structures*, 2016, **25**, 105035, doi: 10.1088/0964-1726/25/10/105035.
[57] Y. Gui, R. Wu, Buckling analysis of embedded thermo-magneto-electro-elastic nano cylindrical shell subjected to axial load with nonlocal strain gradient theory, *Mechanics Research Communications*, 2023, **128**, 104043, doi: 10.1016/j.mechrescom.2023.104043.
[58] S. Sirimontree, C. Thongchom, P. R. Saffari, N. Refahati, P. R. Saffari, T. Jearsiripongkul, S. Keawsawasvong, Effects of thermal environment and external mean flow on sound transmission loss of sandwich functionally graded magneto-electro-elastic cylindrical nanoshell, *European Journal of Mechanics - A/Solids*, 2023, **97**, 104774, doi: 10.1016/j.euromechsol.2022.104774.
[59] M. H. Shojaeefard, H. Saeidi Googarchin, M. Ghadiri, M. Mahinzare, Micro temperature-dependent FG porous plate: free

vibration and thermal buckling analysis using modified couple stress theory with CPT and FSDT, *Applied Mathematical Modelling*, 2017, **50**, 633-655, doi: 10.1016/j.apm.2017.06.022.
[60] A. R. Ashoori, S. A. Sadough Vanini, E. Salari, Size-dependent axisymmetric vibration of functionally graded circular plates in bifurcation/limit point instability, *Applied Physics A*, 2017, **123**, 226, doi: 10.1007/s00339-017-0825-5.
[61] F. Ebrahimi, E. Salari, Effect of non-uniform temperature distributions on nonlocal vibration and buckling of inhomogeneous size-dependent beams, *Advances in Nano Research*, 2018, **6**, 377, doi: 10.12989/anr.2018.6.4.377.
[62] E. Salari, S. Ali Sadough Vanini, A. Ashoori, Nonlinear thermal stability and snap-through buckling of temperature-dependent geometrically imperfect graded nanobeams on nonlinear elastic foundation, *Materials Research Express*, 2020, **6**, 1250j6, doi: 10.1088/2053-1591/ab5e50.
[63] P. R. Saffari, S. Sirimontree, C. Thongchom, T. Jearsiripongkul, P. R. Saffari, S. Keawsawasvong, Effect of uniform and nonuniform temperature distributions on sound transmission loss of double-walled porous functionally graded magneto-electro-elastic sandwich plates with subsonic external flow, *International Journal of Thermofluids*, 2023, **17**, 100311, doi: 10.1016/j.ijft.2023.100311.
[64] R. Saini, R. Lal, Axisymmetric vibrations of temperature-dependent functionally graded moderately thick circular plates with two-dimensional material and temperature distribution, *Engineering with Computers*, 2022, **38**, 437-452, doi: 10.1007/s00366-020-01056-1.
[65] X.-L. Huang, H.-S. Shen, Nonlinear vibration and dynamic response of functionally graded plates in thermal environments, *International Journal of Solids and Structures*, 2004, **41**, 2403-2427, doi: 10.1016/j.ijsolstr.2003.11.012.
[66] Y. S. Li, Buckling analysis of magnetoelectroelastic plate resting on Pasternak elastic foundation, *Mechanics Research Communications*, 2014, **56**, 104-114, doi: 10.1016/j.mechrescom.2013.12.007.
[67] G. G. Sheng, X. Wang, Nonlinear vibration control of functionally graded laminated cylindrical shells, *Composites Part B: Engineering*, 2013, **52**, 1-10, doi: 10.1016/j.compositesb.2013.03.008.
[68] J. Abdolhoseyni, M. Danesh, Sound transmission loss of a sandwich functionally graded cylindrical shell integrated with magneto-electro-elastic patches, *Journal of Sound and Vibration*, 2023, **543**, 117350, doi: 10.1016/j.jsv.2022.117350.
[69] Y. Tadi Beni, F. Mehralian, H. Razavi, Free vibration analysis of size-dependent shear deformable functionally graded cylindrical shell on the basis of modified couple stress theory, *Composite Structures*, 2015, **120**, 65-78, doi: 10.1016/j.compstruct.2014.09.065.
[70] P. R. Saffari, C. Thongchom, T. Jearsiripongkul, P. R. Saffari, S. Keawsawasvong, S. Kongwat, Thermo-vibro-acoustic analysis of pavement under a harmonically rectangular moving load, *International Journal of Thermofluids*, 2023, **20**, 100409, doi: 10.1016/j.ijft.2023.100409.
[71] F. Ebrahimi, E. Salari, Semi-analytical vibration analysis of functionally graded size-dependent nanobeams with various boundary conditions, *Smart Structures and Systems*, 2017, **19**, 243-257, doi: 10.12989/sss.2017.19.3.243.
[72] Y. Heidari, M. Irani Rahaghi, M. Arefi, Free vibration analysis of a porous rotor integrated with regular patterns of circumferentially distributed functionally graded piezoelectric patches on inner and outer surfaces, *Journal of Intelligent Material Systems and Structures*, 2021, **32**, 82-103, doi: 10.1177/1045389x20948608.
[73] Y. Wang, K. Xie, T. Fu, W. Zhang, A unified modified couple stress model for size-dependent free vibrations of FG cylindrical microshells based on high-order shear deformation theory, *The European Physical Journal Plus*, 2020, **135**, 71, doi: 10.1140/epjp/s13360-019-00012-3.
[74] L.-L. Ke, Y.-S. Wang, J. Yang, S. Kitipornchai, The size-dependent vibration of embedded magneto-electro-elastic cylindrical nanoshells, *Smart Materials and Structures*, 2014, **23**, 125036, doi: 10.1088/0964-1726/23/12/125036.

